A Model for Computing Radiation Transport in Non-LTE Plasmas

J.J. MacFarlane, P. Wang, and G.A. Moses

February 1990

UWFDM-822

FUSION TECHNOLOGY INSTITUTE

UNIVERSITY OF WISCONSIN

MADISON WISCONSIN

A Model for Computing Radiation Transport in Non-LTE Plasmas

J.J. MacFarlane, P. Wang, and G.A. Moses

Fusion Technology Institute
University of Wisconsin
1500 Engineering Drive
Madison, WI 53706

http://fti.neep.wisc.edu

February 1990

UWFDM-822

A MODEL FOR COMPUTING RADIATION TRANSPORT IN NON-LTE PLASMAS

J.J. MacFarlane, P. Wang, and G.A. Moses

ABSTRACT

We describe a model based on escape probability techniques to compute radiative transfer in non-LTE plasmas. Atomic rate equations are solved self-consistently with the radiation field for multilevel atomic systems. The frequency- and angle-averaging techniques employed allow for computationally efficient solutions, making the model suitable for coupling with radiation-hydrodynamics codes. We present comparisons of escape probability results with exact solutions for 2-level atomic systems, and present preliminary results for multilevel isothermal, isochoric Al and Ne plasmas.

1. INTRODUCTION

When a plasma is in local thermodynamic equilibrium (LTE), its properties (e.g., internal energy, opacity) depend only on the *local* temperature and density [1]. All atomic processes, whether collisional or radiative, are in detailed balance; i.e., the rate at which each process occurs is exactly balanced by the rate of its inverse process. Collisional processes occur with sufficient frequency that Maxwellian velocity distributions exist for atoms, ions, and electrons. Ionization and excitation populations are prescribed by the well-known Saha equation and Boltzmann statistics, respectively. In addition, the same absolute temperature, T, defines the velocity and population distributions. Only the radiation field may be different than its thermodynamic equilibrium (T.E.) value of $B_\nu(T)$ ($B_\nu \equiv$ Planck function).

The conditions that define local thermodynamic equilibrium have often been invoked — either in whole or in part — in theoretical studies of laboratory or

astrophysical plasmas in order to facilitate solutions to problems. For example, most radiation-hydrodynamics codes that are used to study rapidly changing plasmas use internal energies and opacities that depend only on the local temperature and density, and thus are *independent of the radiation field.* This greatly reduces the computational time required for problems for two reasons. First the level populations and opacities are solved independently of the radiative transfer equation. Second, the plasma properties can be calculated ahead of time and stored in two-dimensional (T, ρ) tables. If a plasma is optically thick, however, so that the populations are affected by photoexcitation and photoionization processes, significant departures from LTE can occur. In such cases, reliable determinations of plasma conditions require more detailed non-LTE analysis. This is particularly true when attempting to diagnose conditions in laboratory plasmas.

During the past decade, several studies [2-4] have shown that high-temperature, moderate-to-high density ($n \sim 10^{16} - 10^{22}$ cm^{-3}) laboratory plasmas can be far from LTE. For instance, Duston and Davis [3] have shown that the radiative properties of plasmas which are optically thick to line radiation are not well-described by either "coronal" or LTE plasmas. This results from the fact that line radiation — particularly that of line cores — is absorbed before it escapes the plasma. This affects both the total intensity of line radiation escaping a plasma and the observed line shapes. More recently, similar conclusions have been reached for inertial confinement fusion (ICF) target chamber plasmas in the density range $n \sim 10^{16} - 10^{18}$ cm^{-3} [5].

The fact that the radiation field can significantly affect the properties of a plasma severely complicates the problem of modelling — and hence developing a better understanding of — laboratory plasmas. This is because the opacities are altered by the photon-induced redistribution of the level populations, which in turn affects the radiation field. Because of this feedback mechanism, the atomic rate equations and radiation field must be evaluated self-consistently. The problem becomes particularly cumbersome when high-Z (Z $\equiv$ atomic number) materials are involved because of the

large number of ionization and excitation levels that must be considered. For these reasons, radiation-hydrodynamics calculations have often neglected the influence of the radiation field on the level populations.

To develop a better understanding of non-LTE plasmas and allow for more reliable simulations of rapidly changing plasmas, Apruzese and his co-workers at the U.S. Naval Research Laboratory proposed a non-LTE radiation transport model based on an escape probability formalism [2,6,7,8]. In this model, an angle- and frequency-averaging technique is used which allows the simultaneous, yet computationally efficient, solution of the radiation field and atomic rate equations. Frequency-averaged escape probability integrals for bound-bound and bound-free profiles are computed and fitted to simple analytic expressions. The model has been extended to cylindrical and spherical geometries by introducing a "mean diffusivity angle," along which the zone-to-zone escape probability is evaluated. Results from this model have been shown to compare very favorably with exact solutions for problems involving a variety of geometries and line profiles.

Because the angle- and frequency-averaging methods employed in this model allow rapid solution of the radiation and atomic rate equations, it can be incorporated inside hydrodynamics codes to study rapidly changing plasmas, such as those created by intense ion or laser beams. With the support of Kernforschungszentrum Karlsruhe (KfK), we are currently developing a similar model at Wisconsin to study ICF fusion-related plasmas; e.g., light ion-produced laboratory plasmas, high-yield target chamber plasmas, and Z-pinch plasma channel formation. We wish to emphasize that the computer coding for the radiative transfer model is being developed in a modular fashion so that it can be easily combined with currently existing radiation-hydrodynamics codes.

Below we provide a description of our non-LTE radiative transfer model. In Section 2, the escape probability model is described in detail. We also include a short discussion of the physical basis for the model, and comparison of model results with exact solutions

for 2-level atomic systems. In Section 3, we present preliminary results for multilevel atomic systems, and comparisons to other calculations. We conclude in Section 4 with a summary of the status of the model/code development, and discuss features that need to be added to the model in the future.

2. OVERVIEW OF ESCAPE PROBABILITY RADIATIVE TRANSFER MODEL

A. Physical Basis

In optically thick non-LTE plasmas, the atomic rate equations must be solved self-consistently with the radiation field because the level populations — and therefore opacities — can be significantly altered through photoexcitation and photoionization processes. Any model that does not account for this coupling can lead to inaccurate results for both energetics and diagnoses of plasma conditions.

A physical understanding of this situation can more readily be attained by considering the case of a 2-level atom. Let n_u and n_l denote the population densities of the upper and lower states, respectively. The rate at which the upper level is populated at a location $\mathbf{r}$ within the plasma is [1]:

$$\begin{aligned}\frac{dn_u(\mathbf{r})}{dt} &= n_l(\mathbf{r})[C_{lu}(\mathbf{r}) + B_{lu}\int \phi_\nu J_\nu(\mathbf{r})d\nu] \\ &\quad - n_u(\mathbf{r})[C_{ul}(\mathbf{r}) + A_{ul} + B_{ul}\int \phi_\nu J_\nu(\mathbf{r})d\nu]\end{aligned} \tag{1}$$

where A_{ul} is the Einstein spontaneous transition probability, C_{lu} is the collisional excitation rate, C_{ul} is the collisional deexcitation rate, B_{lu} and B_{ul} are the Einstein photoexcitation and stimulated emission coefficients, ϕ_ν is the normalized line profile ($\int \phi_\nu d\nu = 1$), and J_ν is the mean intensity of the radiation field. In the escape probability model, we assume the atomic transition rates are much faster than the rate of change of the plasma conditions, so that $dn_u/dt = dn_l/dt = 0$.

The spontaneous emission term in Eq. (1) depends only on the atomic properties of

the plasma. The collisional terms depend on the *local* temperature and density ($T(\mathbf{r})$ and $n(\mathbf{r})$) and the atomic properties. The photoexcitation and stimulated emission terms, however, depend in addition on the radiation field, which is a non-local entity. Thus, the level populations at $\mathbf{r}$ depend on the conditions in other parts of the plasma.

The radiation field throughout a plasma can be determined by solving the radiation transport equation:

$$\frac{1}{c}\frac{\partial I_\nu}{\partial t} + \hat{\mathbf{n}} \cdot \nabla I_\nu = \eta_\nu - \chi_\nu I_\nu, \tag{2}$$

where η_ν is the emission coefficient, χ_ν is the extinction coefficient, c is the speed of light, and $\hat{\mathbf{n}}$ is the unit vector representing the direction of propagation. The mean intensity J_ν in Eq. (2) is the average of the specific intensity, I_ν, over solid angle:

$$J_\nu(\mathbf{r}) = \frac{1}{4\pi} \oint I_\nu(\mathbf{r}, \hat{\mathbf{n}}) d\omega. \tag{3}$$

The major difficulty associated with non-LTE radiation transport is that Eqs. (1) and (2) must be evaluated self-consistently. Since we are here concerned with developing a model that can be used within radiation-hydrodynamics codes to study rapidly changing plasmas, the techniques employed to evaluate these equations cannot require large amounts of computer time. We shall now describe such a method based on probability of escape techniques.

B. Escape Probabilities

The probability that a photon of frequency ν will traverse an optical depth τ_ν before being absorbed is [9]:

$$p_\nu = e^{-\tau_\nu}. \tag{4}$$

The optical depth can also be expressed in terms of the absorption coefficient κ_ν and propagation distance r:

$$\tau_\nu = \int \kappa_\nu(r) dr. \tag{5}$$

The frequency-averaged probability that a photon emitted as a result of a downward transition with an emission profile $\phi_E(\nu)$ is [10]:

$$P_e = \int_0^\infty \phi_E(\nu)\ \exp(-\tau_\nu)\ d\nu, \tag{6}$$

where ϕ_E is normalized such that $\int \phi_E(\nu)d\nu = 1$.

Given the above definitions, one can readily compute the escape probability for Doppler and Lorentz line profiles. For lines, we shall assume complete redistribution [1] of absorbed radiation so that the emission and absorption profiles are identical ($\phi_E = \phi_A = \phi$). The normalized Doppler profile can be written as:

$$\phi(x) = \frac{e^{-x^2}}{\pi^{1/2}\Delta\nu_D}, \tag{7}$$

where

$$x \equiv (\nu - \nu_o)/\Delta\nu_D,$$

$\Delta\nu_D$ is the Doppler width, and ν_o is the line center frequency. For a Lorentz profile,

$$\phi(x) = \frac{4}{\Gamma}\frac{1}{1+x^2}, \tag{8}$$

where

$$x \equiv \frac{4\pi}{\Gamma}(\nu - \nu_o)$$

and Γ is the half-maximum intensity width. Writing τ_ν in Eq. (6) in terms of the line center optical depth τ_c, the frequency-averaged escape probability for bound-bound transitions is:

$$P_e(\tau_c) = \int_0^\infty \phi(\nu)\ \exp(-\tau_c\phi(\nu)/\phi_o)d\nu \tag{9}$$

where $\phi_o \equiv \phi(\nu = \nu_o)$. Equation (9) has been evaluated numerically for Doppler and

Lorentz profiles, and the results have been fitted to analytic expressions [6]. Figure 1 shows both the exact (solid curves) and fitted (dashed curves) escape probabilities as a function of line center optical depth. For Doppler profiles the fitted curves are:

$$P_e(\tau_c) = \begin{cases} 1/(1 + 0.65\ \tau_c + 0.29\tau_c^2), & \tau_c \leq 5.18 \\ 0.5456/[\tau_c(ln\ \tau_c)^{1/2}], & \tau_c > 5.18. \end{cases} \tag{10}$$

The curve fits for a Lorentz profile are:

$$P_e(\tau_c) = \begin{cases} 1/(1 + 0.5857\ \tau_c), & \tau_c \leq 5.18 \\ 1/(\pi\ \tau_c)^{1/2}, & \tau_c > 5.18. \end{cases} \tag{11}$$

Equations (10) and (11) are continuous at $\tau_c = 5.18$, and differ from the exact solutions by a maximum of 4% for Doppler profiles and 8% for Lorentz profiles.

The relative contributions from the line wings to the frequency-averaged escape probability increase as the optical depth increases. This is illustrated in Figure 2, where the frequency-dependent escape probabilities for Doppler and Lorentz profiles are plotted as a function of the scaled frequency for several values of the line center optical depth. Note that as the optical depth increases, the fraction of line core photons escaping the plasma from that depth decreases dramatically. On the other hand, the wing photons can escape because the optical depths in the wings are significantly lower. Note also that radiation escapes more readily from the wings of Lorentz profiles compared to Doppler profiles. This is because Lorentz profiles emit a larger fraction of their radiation from the wings, where reabsorption is less important than in the core.

For bound-free transitions, we use hydrogenic emission and absorption profiles to compute the escape probabilities. The emission profile can be written as [11]

$$\phi_E(\nu) = \frac{\exp(-h\nu/kT_e)}{\nu\ E_1(h\nu_1/kT_e)}, \qquad \nu \geq \nu_1, \tag{12}$$

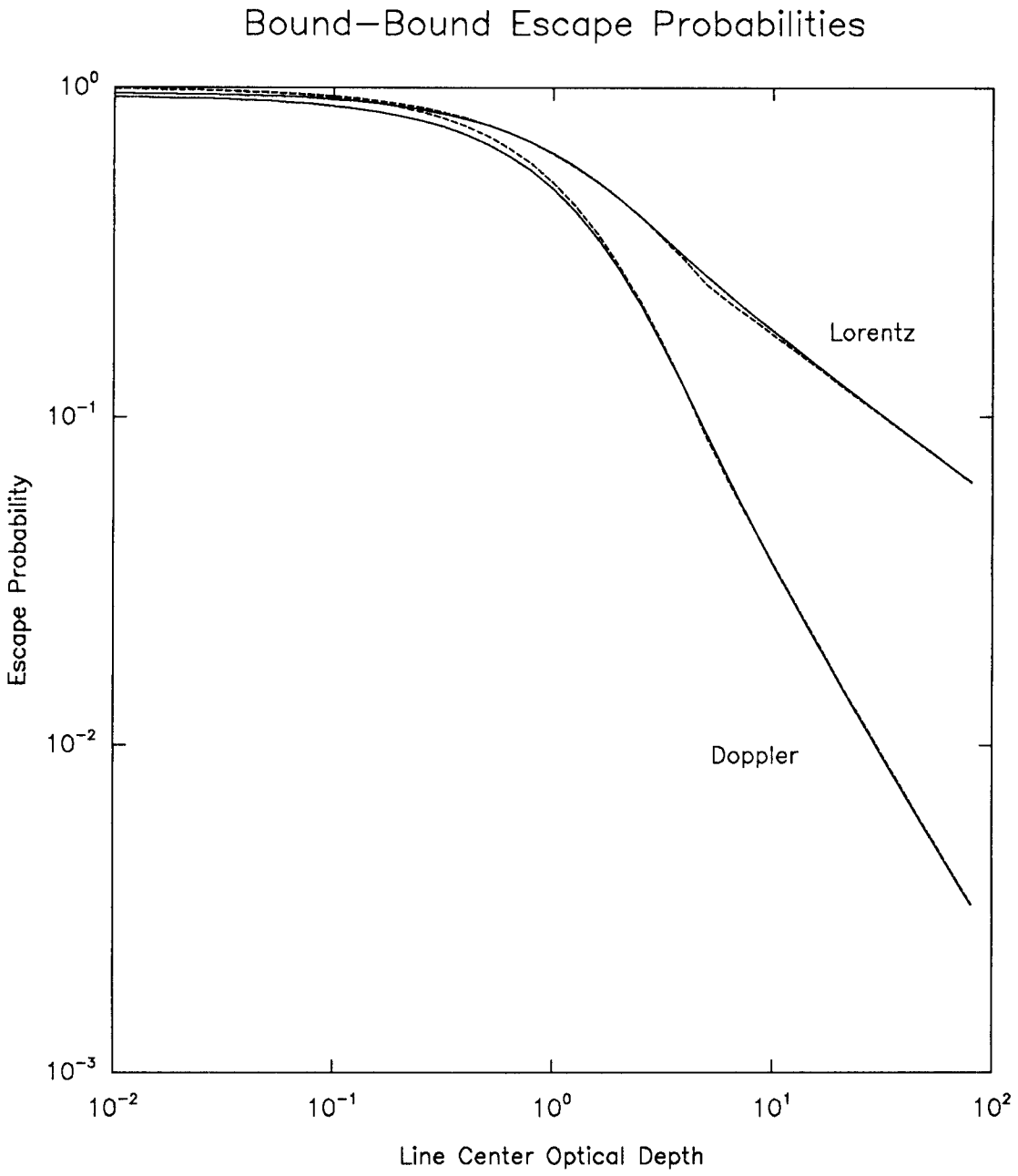

Figure 1. Frequency-averaged bound-bound escape probabilities for Doppler and Lorentz line profiles. Exact solutions (solid curves) are compared with fitted (dashed) curves.

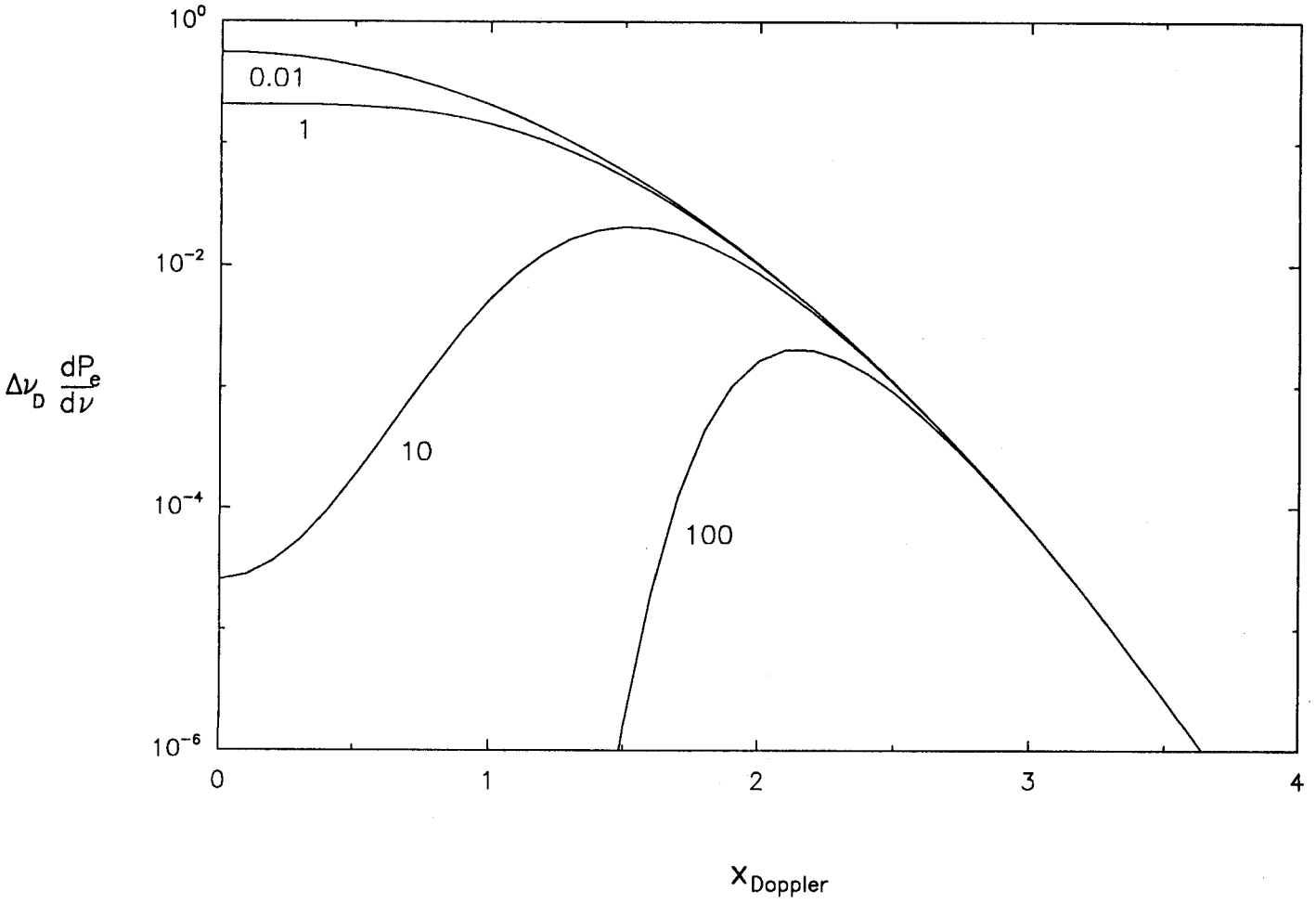

Figure 2(a). Doppler profile escape probability as a function of scaled frequency for line center optical depths of 0.01, 1, 10, and 100. The line center is at $x = 0$.

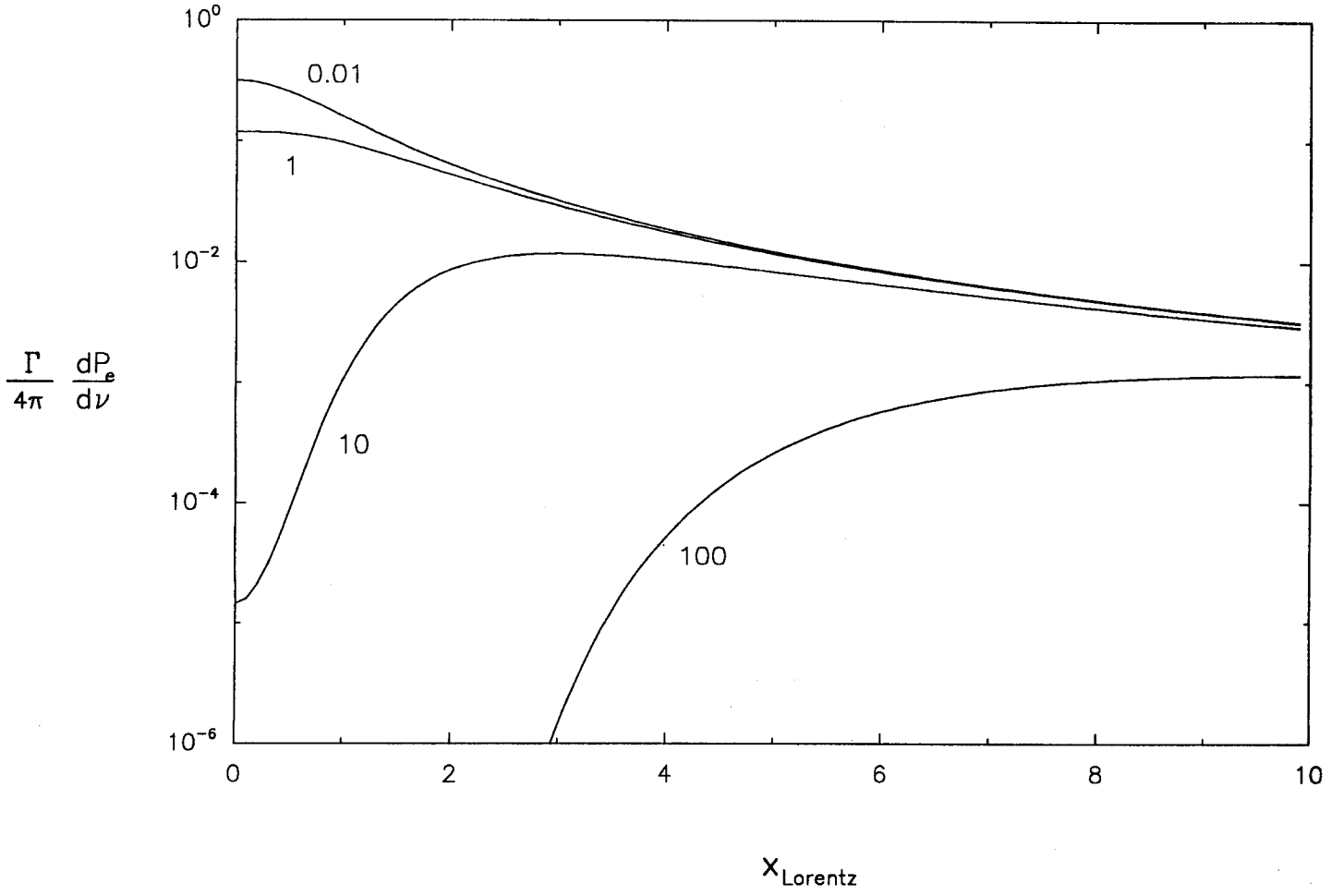

Figure 2(b). Lorentz profile escape probability as a function of scaled frequency for line center optical depths of 0.01, 1, 10, and 100. The line center is at $x = 0$.

and the absorption profile is

$$\phi_A(\nu) = \phi_o(\nu_1/\nu)^3, \qquad \nu > \nu_1. \tag{13}$$

The quantity ν_1 is the photoionization cutoff frequency, $\phi_o \equiv \phi(\nu = \nu_1)$, T_e is the electron temperature, $E_1(x)$ represents the first exponential integral, h is Planck's constant, and k is Boltzmann's constant. The bound-free frequency-averaged escape probability is then:

$$P_e(\tau_o) = \frac{1}{E_1(\alpha_o)} \int_1^\infty dy\, y^{-1} \exp\{-\alpha_o y - \tau_o y^{-3}\}, \tag{14}$$

where $y \equiv (\nu/\nu_1)$, $\alpha_o \equiv (h\nu_1/kT_e)$, and τ_o is the optical depth at the cutoff frequency ν_1.

Equation (14) has been evaluated numerically for a variety of τ_o and α_o. Results are shown in Figure 3 (solid curves). Also shown are the curve fits (dashed curves) to the numerical results, which are accurate to within 40% for the range of α_o and τ_o shown. It is seen that for a constant optical depth, the probability of escape increases as the electron temperature increases. This occurs because as the temperature — and hence the mean thermal speed of electrons — increases, the photons emitted by recombinations tend to have energies farther above the threshold energy ($KE(e^-) \longrightarrow h(\nu - \nu_1)$). Thus, as the photon energies become higher, the probability of photoabsorption decreases, and the escape probability increases.

C. Coupling Coefficients

Solution of the atomic rate equations requires information on the (non-local) radiation field. For instance, the photoexcitation rate at one location in the plasma can depend on the conditions in other regions of the plasma. In the context of the escape probability model, the number of photoexcitations that occur in zone a per unit time can

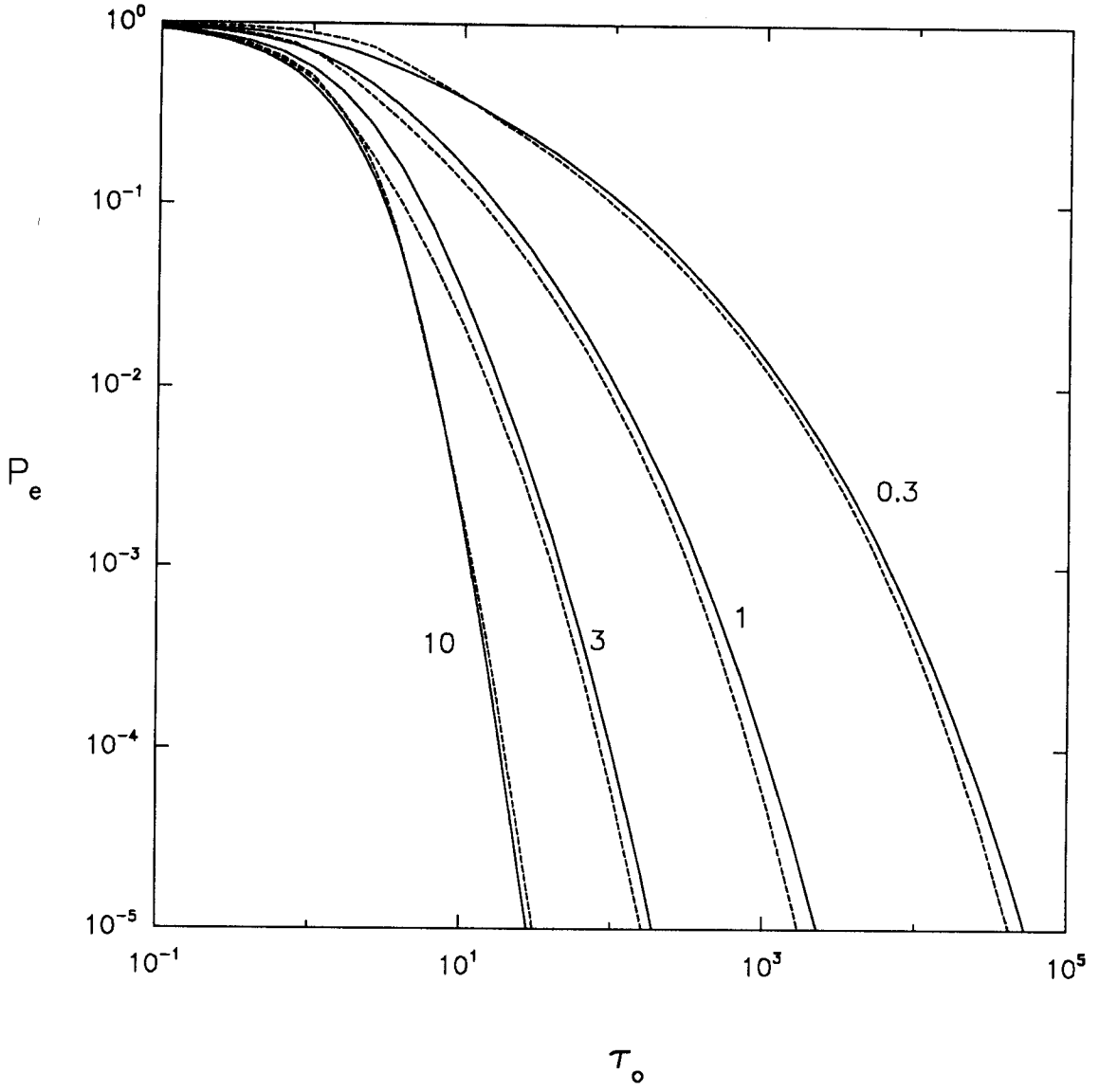

Figure 3. Frequency-averaged bound-free escape probabilities vs. optical depth at the photonionization edge. Curve labels correspond to different values of $\alpha_o \equiv h\nu_1/kT_e$.

be written as

$$\frac{dN_u^a}{dt} = \sum_{e=1}^{N_z} A_{ul} N_u^e Q^{ea} \tag{15}$$

where Q^{ea} is the probability a photon emitted in zone e is absorbed in zone a. We shall refer to the set of Q's as "coupling coefficients." The quantity N_u^e is the total number of excited state atoms in zone e. Thus, the product $N_u^e\ A_{ul}$ is the total number of photons per unit time originating in zone e.

We shall now discuss methods for evaluating coupling coefficients in planar, cylindrical, and spherical geometries. Consider first the 1-D planar geometry shown in Figure 4. The distance traversed as a photon travels from point 1 to point 2 is z_{12}/μ, where $\mu \equiv cos\ \theta$ and θ is the angle between the direction of propagation and the normal to the slab surface. In this geometry, the angle- and frequency-averaged escape probability, $\overline{P_e}$, can be computed directly:

$$\overline{P_e}(\tau_c) = \int_0^1 P_e(\tau_c/\mu) d\mu, \tag{16}$$

where P_e is the frequency-averaged escape probability described above. The probability a photon emitted in zone e traverses a depth τ_B between zones e and a, and is then absorbed in zone a is

$$Q^{ea} = \frac{1}{2\tau_e} \int_0^{\tau_e} [\bar{P}_e(\tau_B + \tau) - \bar{P}_e(\tau_B + \tau_a + \tau)] d\tau. \tag{17}$$

Note that τ_e, τ_B, and τ_a are the optical depths in the direction normal to the slab surface. The first term within the integral represents the probability a photon will get to the nearer surface of zone a without being absorbed, while the second term represents the probability the photon is absorbed before exitting the surface farther from zone e. The coupling coefficients are rapidly determined from analytic expressions — Eqs. (10), (11), (16), and (17).

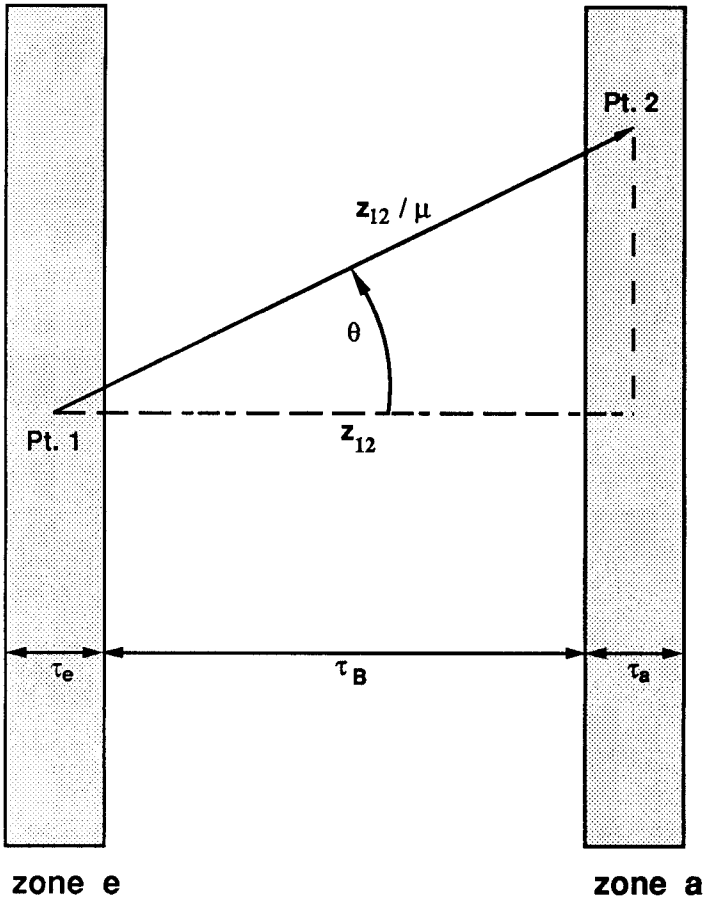

Figure 4. Schematic illustration of photon transport in planar geometries.

Results for a 2-level atom can be compared with exact solutions. Assuming steady-state conditions, the 2-level rate equation in the escape probability model becomes (see Eq. (1)):

$$\frac{dN_u^i}{dt} = N_l^i\ C_{lu}^i + \sum_{j=1}^{N_D} A_{ul}\ N_u^j\ Q^{ji} - N_u^i\ (A_{ul} + C_{ul}^i) = 0, \tag{18}$$

where i and j refer to the zone indices. The level populations for each of the N_D zones are determined simultaneously by solving an $N_D \times N_D$ matrix.

It is often useful to write the rate equations in terms of the source function S_ν and a "quenching parameter" P_Q. This allows the rate equation to be written in a more general form, and eliminates the need for computing rate coefficients for a particular transition, temperature, and density. The quenching parameter is defined by [12]

$$P_Q = \frac{C_{ul}}{C_{ul} + A_{ul}(1 - e^{-\alpha})^{-1}}, \tag{19}$$

where $\alpha = h\nu_o/kT_e$, and $h\nu_o$ is the transition energy. Substituting Eq. (19) into (18), the rate equation becomes:

$$\begin{aligned} N_{tot}^a = N_u^a \left[1 + \frac{g_l}{g_u}(e^\alpha + P_Q'(e^\alpha - 1))\right] \\ - \frac{g_l}{g_u} P_Q'(e^\alpha - 1) \sum_{e=1}^{N_D} n_u^e\ Q^{ea}, \end{aligned} \tag{20}$$

where $P_Q' \equiv \frac{1-P_Q}{P_Q}$ and g_l and g_u represent the statistical weights of the lower and upper levels, respectively. The source function can be written as [1]:

$$S_\nu \equiv \eta_\nu/\kappa_\nu = n_u\ A_{ul}/(n_l\ B_{lu} - n_u\ B_{ul}), \tag{21}$$

where η_ν and κ_ν represent the emissivity and absorption coefficient, respectively. Using the relation between the upward and downward collisional rates, $C_{lu} = C_{ul}(g_u/g_l)e^{-\alpha}$, the source function for an isothermal (α = constant) plasma is:

$$S_\nu^i = B_\nu P_Q \left[1 - (1 - P_Q) \sum_{j=1}^{N_D} Q^{ji} \left(\frac{N_u^j}{N_u^i} \right) \right] . \tag{22}$$

Equations (21) and (22) specify the unique solution of the source function for a given P_Q and total line center optical depth.

Apruzese et al. [2] and Apruzese [6] showed that the source function — and therefore population distributions — determined using the escape probability model compare quite favorably with exact solutions. We have also compared results from our calculations with the exact solution for several cases. Figures 5(a) through 5(c) show results for several values of P_Q and total optical depth. The dashed curves represent the exact solutions [12]. Note that for both Doppler and Lorentz profiles, the accuracy of the escape probability model is quite good over a wide range of parameters. Using 75 mesh points, typical errors are $\sim$ 10 - 20%, with a maximum of about 25%. This suggests that errors introduced in using angle- and frequency-averaging escape probabilities using a reasonable number of mesh points is $\sim$ a few tens of percent. This degree of error is comparable to the level of uncertainty associated with the atomic rate coefficients, and is significantly less than errors introduced by neglecting the effects of the radiation field on the level populations (see comparisons with diffusion results below).

The results in Figure 5 can be understood as follows. When $P_Q \ll 1$, the spontaneous emission rate is much greater than the collisional deexcitation rate. Thus, when a photon is absorbed, it is usually reemitted by a spontaneous emission and travels another mean-free-path before being reabsorbed. This process can happen many times before the photon either escapes the plasma or is destroyed. "Destruction" occurs when

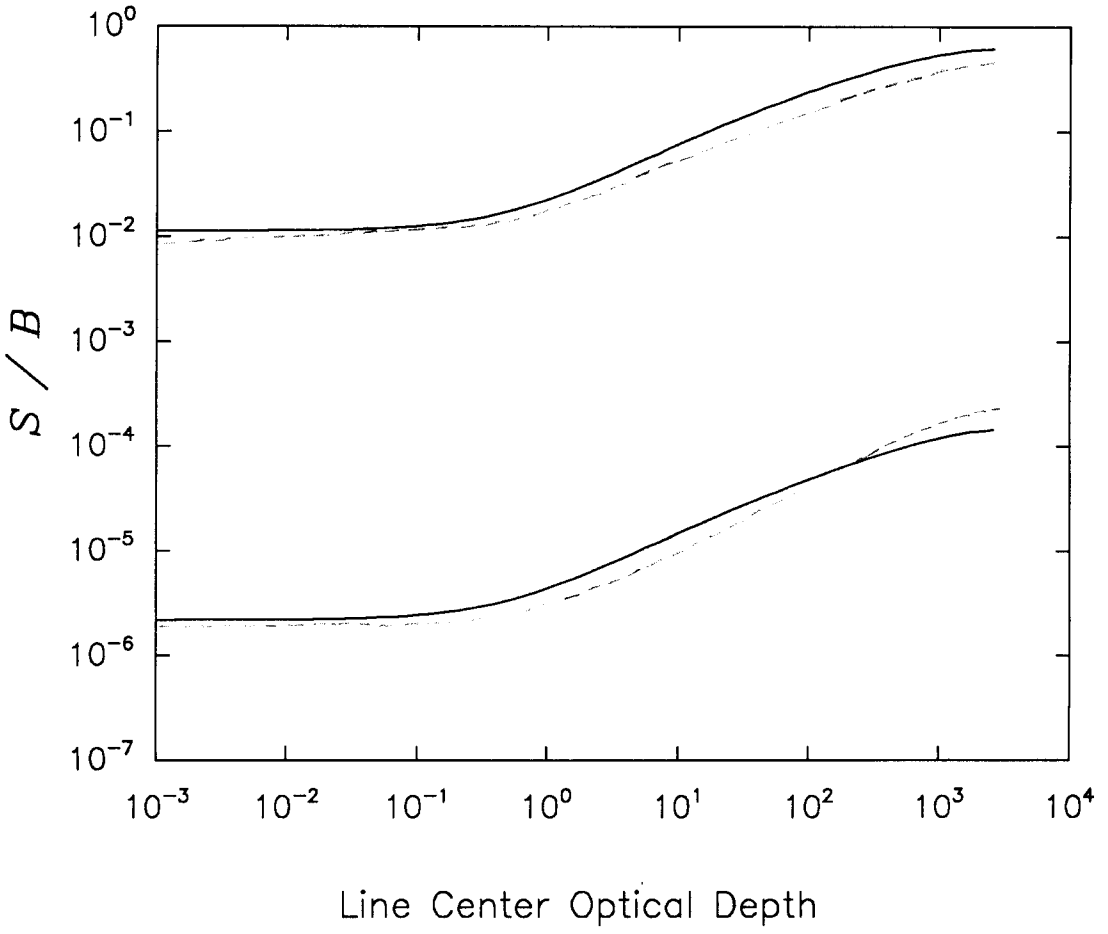

Figure 5(a). Ratio of source function to Planck function for 2-level atoms with Doppler profiles in planar slab. Values of the quenching parameter are $P_Q = 10^{-4}$ (top) and $P_Q = 10^{-8}$ (bottom). The total slab optical depth is 2.82×10^3. Escape probability results (solid curves) are in good agreement with exact solutions (dashed curves).

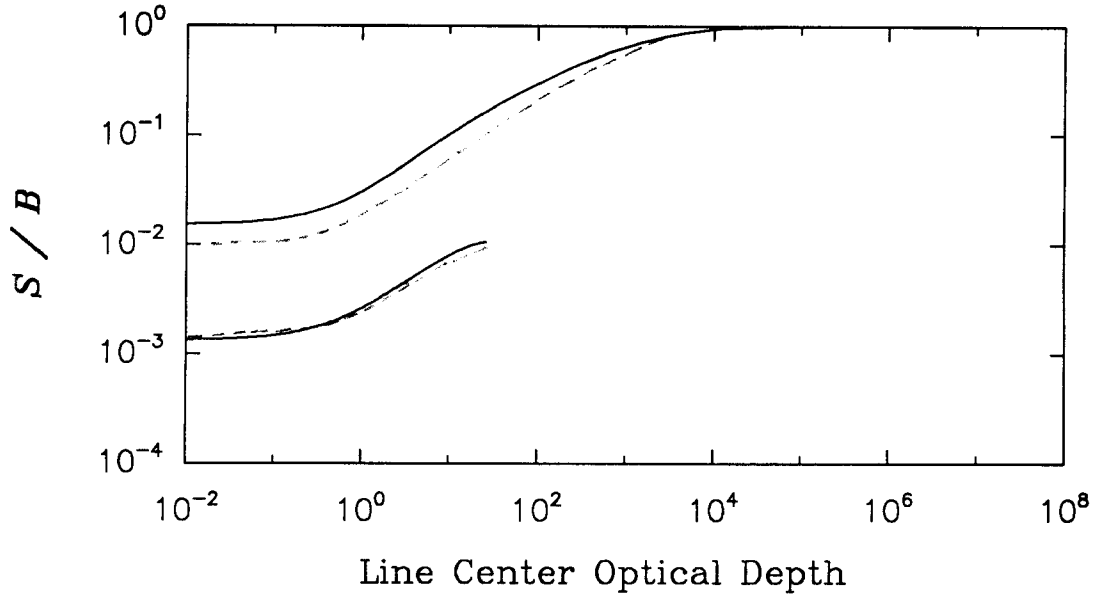

Figure 5(b). Same as Fig. 5(a), but with optical depths of 2.82×10^7 (top) and 28.2 (bottom). $P_Q = 10^{-4}$ for all curves.

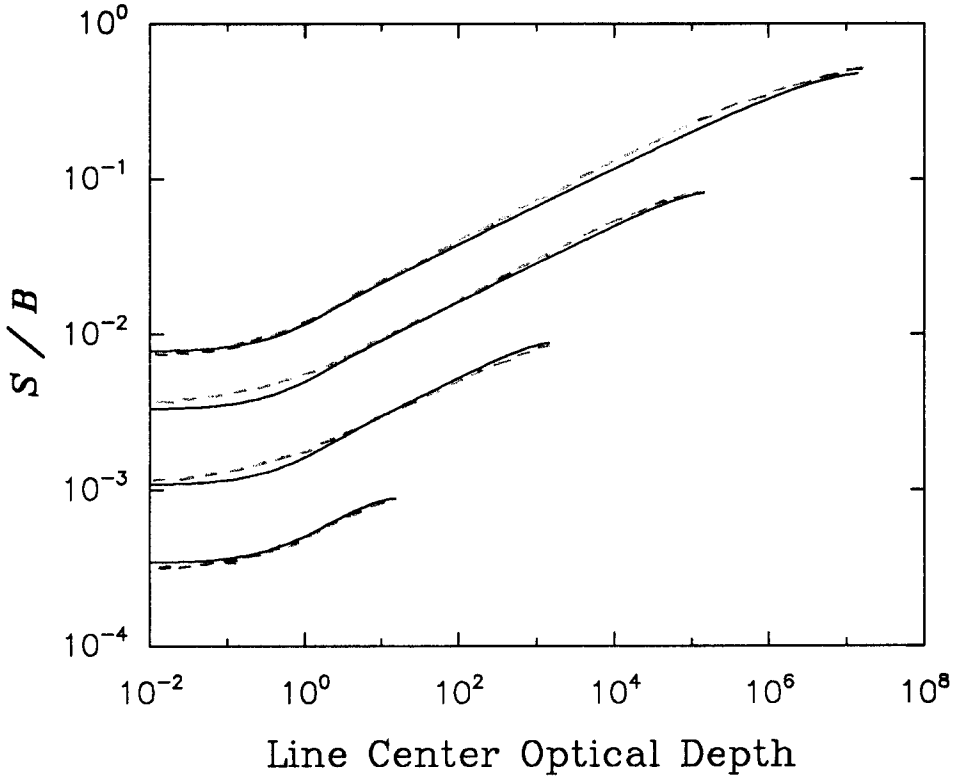

Figure 5(c). Same as Fig. 5(a), but for Lorentz profiles. Total slab optical depths are 1.59×10^7 (top), 1.59×10^5, 1.59×10^3, and 1.59×10^1 (bottom). $P_Q = 10^{-4}$ for all curves.

the energy of the photon is deposited in the plasma thermal energy budget, either as a result of a collisional deexcitation or an absorption by the continuum. As the optical depth increases, the probability a photon will be destroyed before it escapes increases.

Figures 5(b) and 5(c) show that for a given quenching parameter the source function approaches B_ν at large optical depths. This "thermalization depth" is $\Lambda \sim P_Q^{-1}$ for a Doppler profile and $\Lambda \sim P_Q^{-2}$ for a Lorentz profile [12]. At smaller optical depths, photons are able to escape at the plasma boundaries, and S_ν becomes less than B_ν. When the total optical depth is much less than the thermalization depth, photons from throughout the slab can escape, and the plasma is "effectively thin." Figure 5(a) shows that for a given total optical depth, the source function departs more from LTE (where $S = B$) as the quenching parameter decreases. This occurs because the probability of a destructive collisional deexcitation is smaller, and photons can more readily scatter out through the plasma.

For the 2-level atom, the ratio of the upper to lower population in zone i given by:

$$\left(\frac{N_u}{N_l}\right)^i = \frac{g_u}{g_l}\left(\frac{(S_\nu^i/B_\nu)}{(S_\nu^i/B_\nu)+(e^\alpha-1)}\right). \tag{23}$$

Thus, as S_ν/B_i decreases near the edge of the slab, the relative population for the excited level decreases. Note that as $S_\nu \longrightarrow B_\nu$ in Eq. (23), the relative populations are given by Boltzmann statistics.

Evaluation of the coupling coefficients in cylindrical and spherical geometries is more difficult because Eq. (16) is not valid and angle-averaged escape probabilities cannot be computed directly. For these geometries, it was found [6] that introducing a "mean diffusivity angle," $\bar{\theta} \equiv \cos^{-1}\bar{\mu}$, for which

$$P_e\left(\frac{\tau}{\bar{\mu}}\right) \cong \int_0^1 P_e\left(\frac{\tau}{\mu}\right) d\mu, \tag{24}$$

leads to solutions that compare reasonably well with exact solutions. The meaning of the mean diffusivity angle is clarified in Figure 6. The quantities τ_e, τ_a, and τ_B again represent the line center optical depths of the emitting and absorbing zones and the depth between them, respectively. In this case, however, the optical depths are computed along the ray defined by $\bar{\theta}$ and the midpoint of the emitting zone.

It can also be seen from Figure 6 that additional geometrical complications arise when the absorbing zone is inside the emitting zone. To overcome this, while at the same time improving computational efficiency, we take advantage of the reciprocity relation:

$$N^i Q^{ij} = N^j Q^{ji}, \tag{25}$$

where N^i and N^j are the total number of absorbing atoms in zones i and j, respectively. (A proof of this relation is given in Ref. [6]). Thus, in cylindrical and spherical geometries the coupling coefficients are given by:

$$Q^{ea} = \frac{1}{\tau_e} \int_0^{\tau_e} [P_e(\tau_B + \tau) - P_e(\tau_B + \tau_a + \tau)] d\tau, \tag{26}$$

where P_e is the non-angle-averaged escape probability. The Q^{ea} are calculated using Eq. (26) only for the cases when the absorbing zone is at a larger radius than the emitting zone. Otherwise, the reciprocity relation (Eq. (25)) is used.

It has been shown [6] that using $\bar{\mu} = 0.51$ leads to solutions for 2-level atoms that are accurate to within 25% for a wide range of total optical depths. In Figures 7 and 8, we compare results from our 2-level atom calculations with "exact" solutions for Doppler profiles in cylindrical [13] and spherical [14] geometries (in the cylindrical case, the "exact" curves correspond to results from Monte Carlo calculations). The spherical case corresponds to a hollow sphere with an inner radius of $R = 1$ and outer radius ranging from $R = 3$ to 300. The Planck function and absorption coefficient both decrease

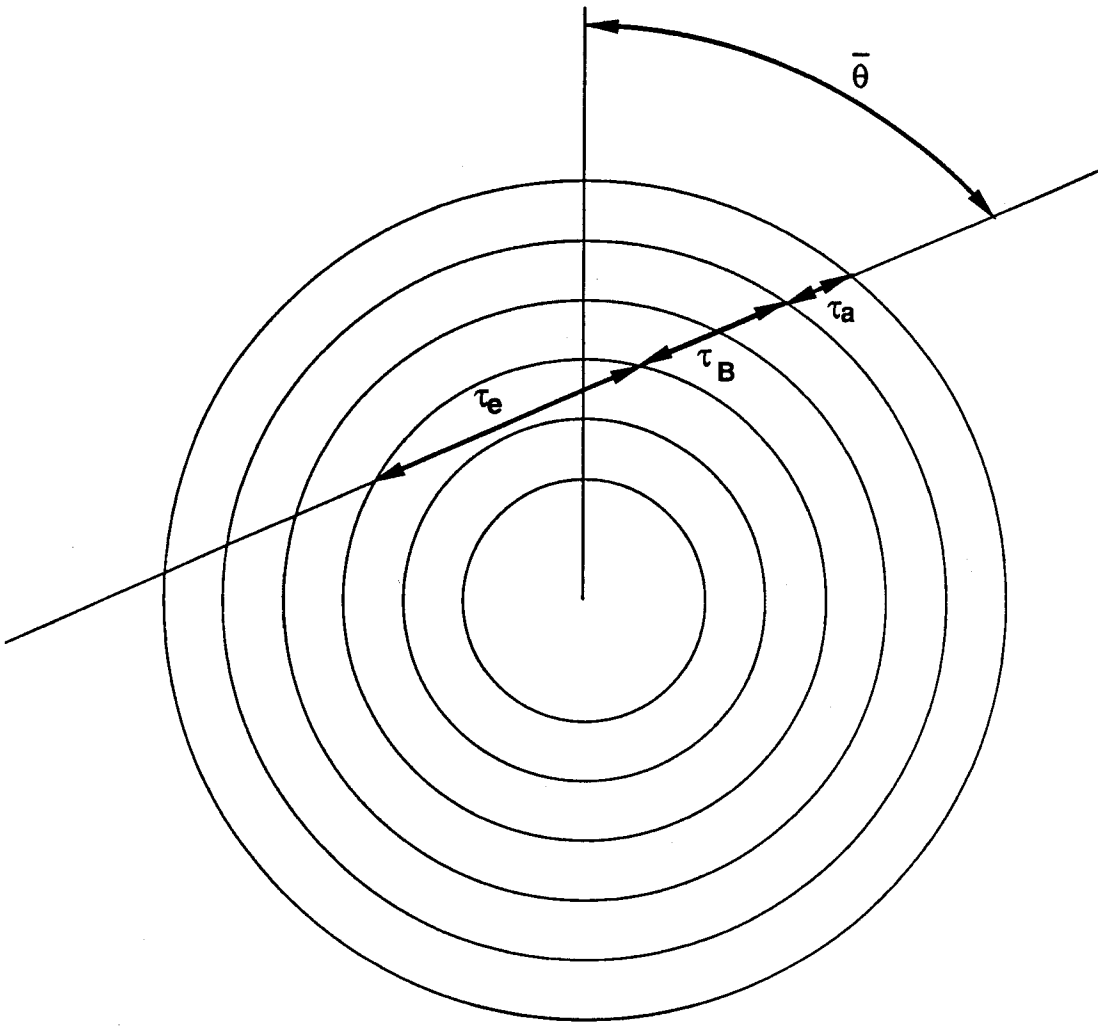

Figure 6. Schematic illustration of photon transport in cylindrical and spherical geometries.

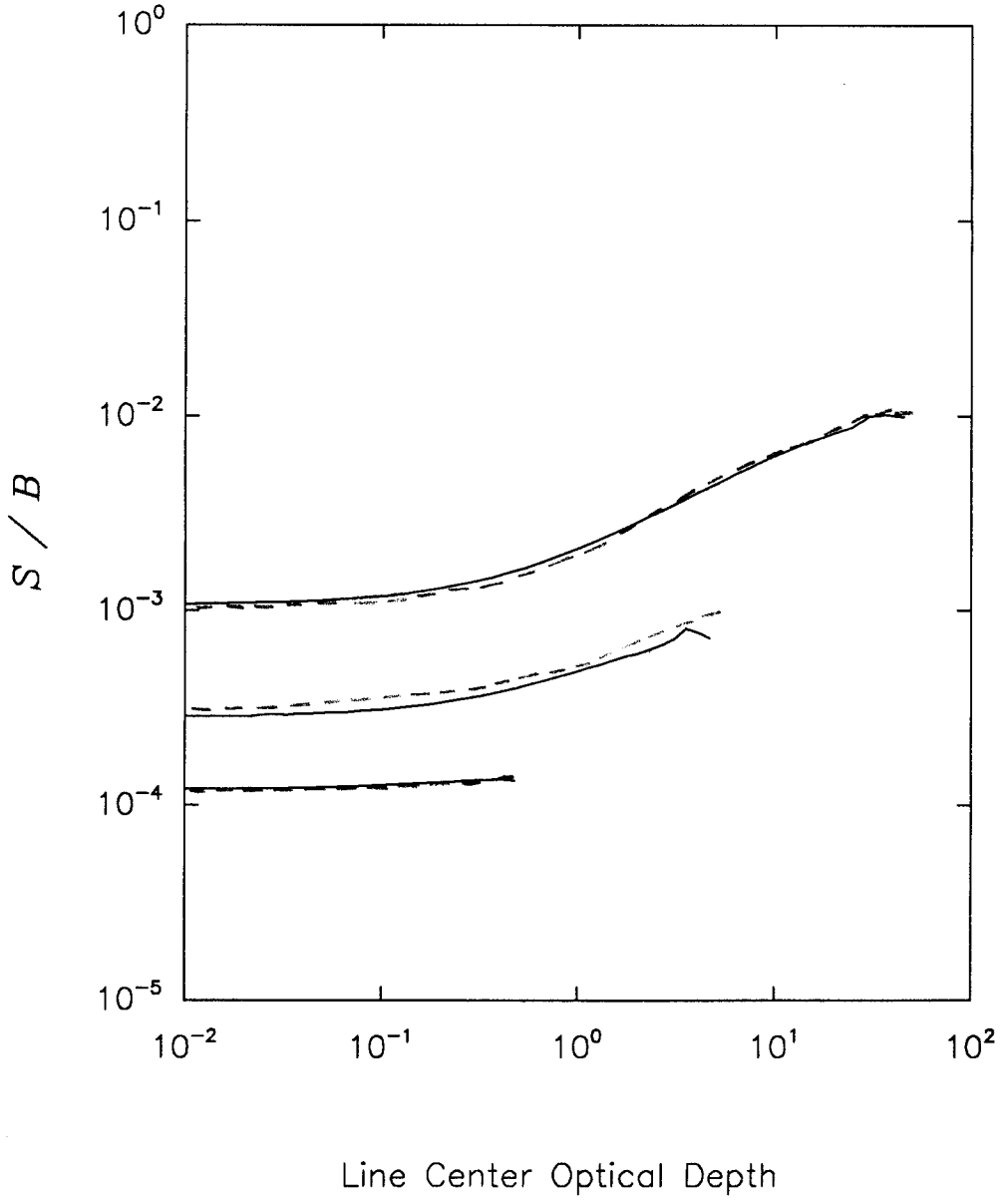

Figure 7. Ratio of source function to Planck function for 2-level atoms with Doppler profiles in cylindrical geometries. The Planck function and absorption coefficient are assumed to be spatially uniform and $P_Q = 10^{-4}$ for all curves. The top, center, and bottom curves correspond to total line center optical depths of 50, 5, and 0.5, respectively, in the radial direction.

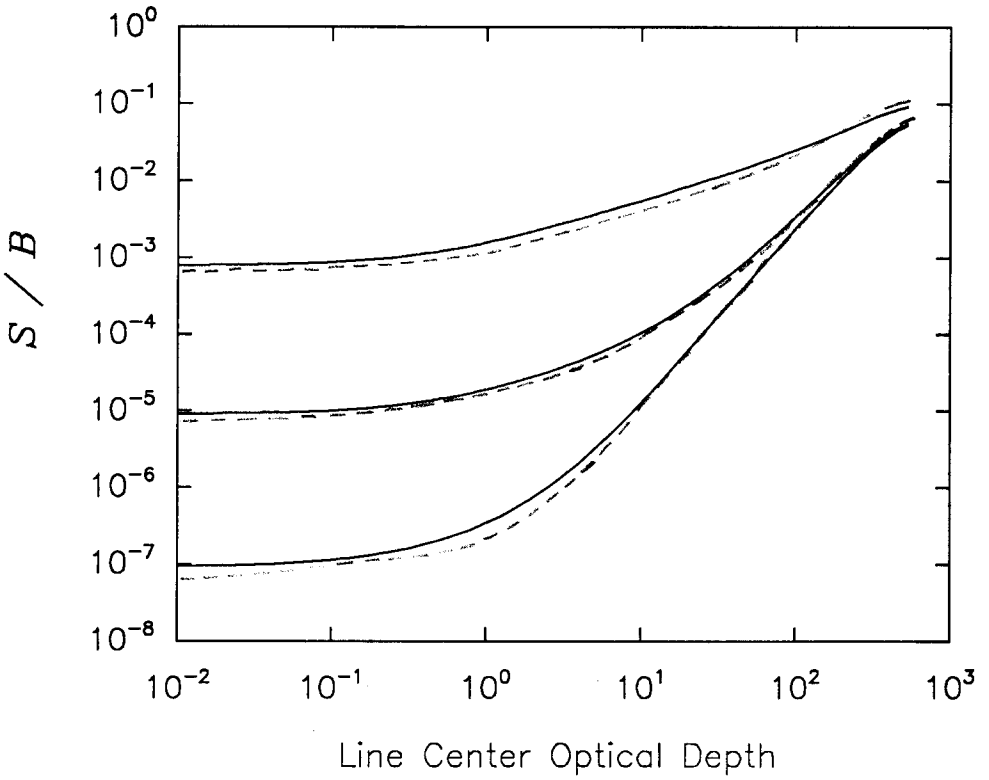

Figure 8. Ratio of source function to Planck function for 2-level atoms with Doppler profiles in spherical geometries. Both the Planck function and absorption coefficient are assumed to decrease in the radial direction as r^{-2}. The radius of the inner boundary of the hollow sphere is $R = 1$ in each case. The radius of the outer boundary is $R = 3, 30$, and 300 for the top, center, and bottom curves, respectively. In each case, the total optical depth is $564 (= 10^3/\pi^{1/2})$ and $P_Q = 10^{-4}$.

as r^{-2}, while $P_Q = 10^{-4}$ for all cases. For the cylindrical case, B and k are held constant throughout the plasma, and the total line center optical depth in the radial direction was varied from 0.5 to 50. Again, the escape probability results are seen to be in good agreement with results from exact calculations.

D. Rate Equations for Multilevel Atomic Systems

For multilevel atomic systems, the steady-state rate equation for level i is:

$$\frac{dn_i}{dt} = -n_i \sum_{j \neq i}^{N_L} W_{ij} + \sum_{j \neq i}^{N_L} n_j W_{ji} = 0, \tag{27}$$

where W_{ij} and W_{ji} are the depopulating and populating rates between levels i and j, and N_L represents the total number of levels in the system. For upward transitions ($i < j$):

$$W_{ij} = B_{ij}\bar{J}_{ij} + n_e C_{ij} + n_e \gamma_{ij} + \beta_{ij}, \tag{28}$$

while for downward transitions ($i > j$):

$$W_{ij} = A_{ij} + B_{ij}\bar{J}_{ij} + n_e D_{ij} + n_e \alpha_{ij} + n_e^2 \delta_{ij}, \tag{29}$$

where n_e is the electron density and $\bar{J}_{ij} \equiv \int \phi_{ij}(\nu) J_\nu d_\nu$. The rate coefficients for the various transitions are represented by:

A_{ij} = spontaneous emission

B_{ij} = stimulated absorption ($i < j$) or emission ($i > j$)

C_{ij} = collisional excitation

D_{ij} = collisional deexcitation

α_{ij} = radiative plus dielectronic recombination

β_{ij} = photoionization

γ_{ij} = collisional ionization

δ_{ij} = collisional recombination.

In the escape probability formalism, the stimulated absorption and emission rates are written in terms of the coupling coefficients, so that:

$$n_j^a\ B_{ji}\ \bar{J}_{ij} - n_i^a\ B_{ij}\ \bar{J}_{ij} = \begin{cases} -A_{ji} \sum_{e=1}^{N_D}\ n_j^e\ Q_{ji}^{ea}, & (i < j) \\ A_{ij} \sum_{e=1}^{N_D}\ n_i^e\ Q_{ij}^{ea}, & (i > j) \end{cases} \tag{30}$$

where the superscripts e and a refer to the emitting and absorbing zones, respectively, and N_D is the number of spatial zones. Note that the coupling coefficients in Eq. (30) contain corrections for stimulated emission. In practice, this is accomplished by evaluating the Q_{ij}^{ea} using optical depths which include stimulated emission effects. For example, the line center optical depth for the transition $l \longrightarrow u$ in zone a is:

$$\tau_{c,ul}^a = (\Delta r)^a \cdot [n_l^a - (g_l/g_u)\ n_u^a]\ \alpha_{ul}^a(\nu = \nu_o), \tag{31}$$

where $\alpha(\nu = \nu_o)$ is the absorption cross-section at the line center.

Equation (27) represents a set of $N_L \times N_D$ coupled rate equations. For each spatial zone, there are $N_L - 1$ independent equations. To prevent trivial solutions (all $n_i = 0$), the conservation of mass equation for each zone is used:

$$n_{tot} = \sum_{i=1}^{N_L} n_i, \tag{32}$$

where n_{tot} is the total number density of particles in a given zone.

At present, the coupled set of rate equations is solved using the LINPACK linear algebra package [15]. The overall method of solution is as follows:

1. Make initial guess for population distributions.

2. Compute coupling coefficients for transitions of interest.
3. Compute coefficients for grand $[(N_L \cdot N_D) \times (N_L \cdot N_D)]$ matrix.
4. Solve grand matrix for level populations.
5. If new populations are consistent with those used to compute coupling coefficients, calculation is complete; otherwise go back to step 2.

The above iteration procedure is called Λ-iteration because it computes the radiation field using populations from the previous iteration step. Up to this point, the above solution procedure has worked satisfactorily for the rather simple problems we have examined. We expect somewhat more refined techniques, such as those discussed in Ref. [8], can be used to accelerate convergence. In addition, it may be worthwhile to explore using iterative techniques that have recently been developed to accelerate convergence in studies concerning radiation transport in astrophysical plasmas [16-18].

E. Radiative Power Emitted by a Plasma

To predict the radiative flux at a detector, the intensity of radiation escaping the entire plasma must be computed. To do this, we compute the escape probability for each zone and transition using the coupling coefficients that have been previously calculated for determining the level populations. The probability a photon emitted in zone e will escape the entire plasma is:

$$PE_{ij}^{e} = 1 - \sum_{a=1}^{N_D} Q_{ij}^{ea}, \tag{33}$$

where the subscript ij refers to the transition states. The total bound-bound power is then given by:

$$P_{bb} = \sum_{i>j} \sum_{e=1}^{N_D} N_i^e \; A_{ij} \; PE_{ij}^e \; \Delta E_{ij}, \tag{34}$$

where N_i^e is the population of level i (upper state) in zone e, A_{ij} is the spontaneous decay rate, and ΔE_{ij} is the transition energy. For bound-free emission, the total power escaping

the plasma is:

$$P_{bf} = \sum_{i>j} \sum_{e=1}^{N_D} N_i^e \, (\alpha^*)_{ij}^e \, n_e^e \, PE_{ij}^e \, \Delta E_{ij}^*, \tag{35}$$

where $(\alpha^*)^e$ is the radiative recombination rate in zone e, n_e^e is the electron density in zone e, and ΔE_{ij}^* is the ionization potential. Using the above expressions, the escape probability model will be able to predict high resolution spectra from laboratory plasma experiments.

3. SAMPLE RESULTS FOR ISOTHERMAL, ISOCHORIC PLASMAS

We have performed calculations using our non-LTE radiative transfer model for 2 classes of problems: Al plasmas with densities $\sim 10^{19} - 10^{23}$ cm^{-3} and Ne plasmas with densities $\sim 10^{16} - 10^{18}$ cm^{-3}. For the Al calculations, we selected conditions such that we can compare our results directly with previously published results. This allows us to assess the reliability of our computer code. For the Ne calculations, we have selected conditions that are relevant to ICF target chamber plasmas (e.g., Z-pinch plasma channel formation for ion beam transport and microfireballs created by ICF target explosions). The primary objectives of this set of calculations was to test our model over an extended density range and in spherical geometries, and to get a preliminary assessment of the importance of non-LTE effects in target chamber plasmas.

We shall examine the results from our Al calculations in somewhat greater detail than the Ne calculations, and they will be compared with previously published calculations. Much of the discussion of the Al results also applies to the Ne results. Other than the nuclear charge, the major difference between the two sets of calculations is that the Ne plasmas considered are several orders of magnitude lower in density and larger in size. The optical depths of the Al and Ne plasmas span a similar range.

For the multilevel calculations described in this section, we have used atomic data computed using a combination of Hartree-Fock and semiclassical methods. We shall only briefly summarize these methods here, as a detailed description will be

presented elsewhere [19]. Hartree-Fock methods are used to compute energy levels, oscillator strengths, and photoionization and radiative recombination rates. Collisional excitation and deexcitation rates and collisional ionization and recombination rates are calculated using a combination of semiclassical impact parameter, Born-Oppenheimer, and distorted wave models [20,21]. Dielectronic recombination rates are computed using the Burgess-Mertz model [22] in conjunction with Hartree-Fock energies and oscillator strengths. Forbidden and spin flip transition rates are determined from distorted wave calculations [21]. Because the escape probability radiation transport model will be a powerful tool for diagnosing time-dependent conditions in non-LTE plasmas, it is important that reliable atomic physics data be used.

Let us first consider the case of an optically thick Al planar plasma with a uniform density of $n = 1 \times 10^{19}$ cm^{-3} and uniform temperature of $T = 600$ eV. At this density and temperature, the Al is predominantly in the H-like (Al XIII) and He-like (Al XII) ionization stages. The level structure for this calculation, which is similar to that used by Apruzese et al. [2], is shown in Figure 9. In all, 3 ionization stages were considered with a total of 14 energy levels. The number of spatial zones was $N_D = 10$, and the total slab thickness was 0.15 cm. For this and other calculations in this section, photoionization effects have been neglected. Previous calculations [3] indicate that photoionization has little effect on the level population at these densities.

Even when the temperature and density are uniform throughout a plasma, the level populations can vary substantially with position because of the non-uniform radiation field. This is shown in Figure 10, where the populations for the Al XII and Al XIII stages are shown as a function of distance from the slab center (solid curves). Note that for some levels (e.g., 1s 2p ^{1}P (Al XII) and $n = 2$ (Al XIII)) the excited state populations decrease by a factor of up to 4 to 7 near the plasma boundary. This occurs because of the lack of radiation incident on the outer boundaries of the plasma. There is a relatively small gradient in the population of the 1s 2p ^{1}S level for Al XII because the transition

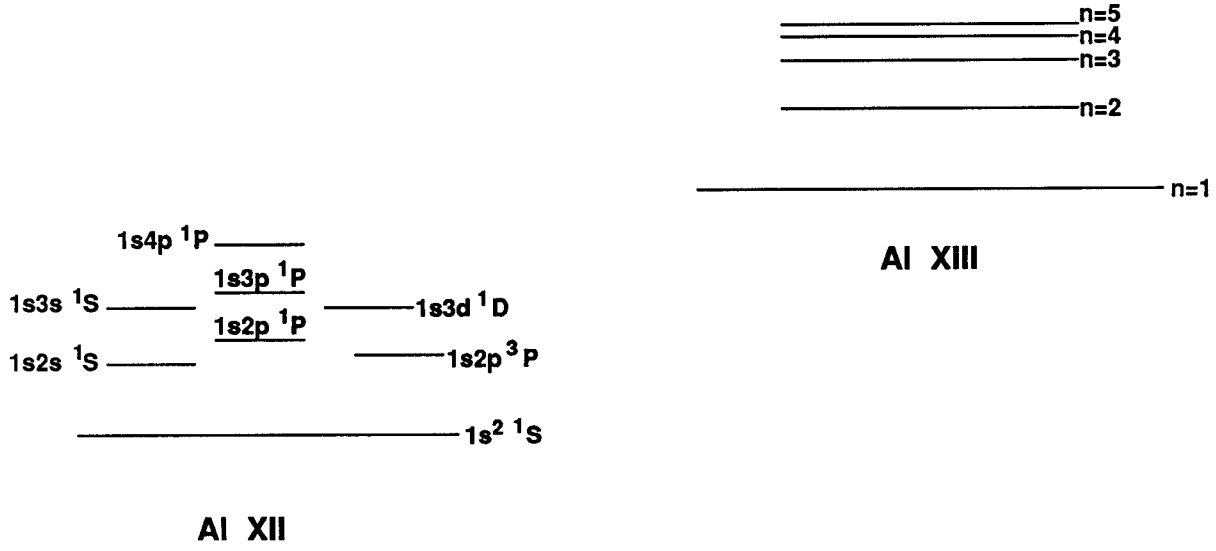

Figure 9. Level structure for the atomic states of Al XII and Al XIII.

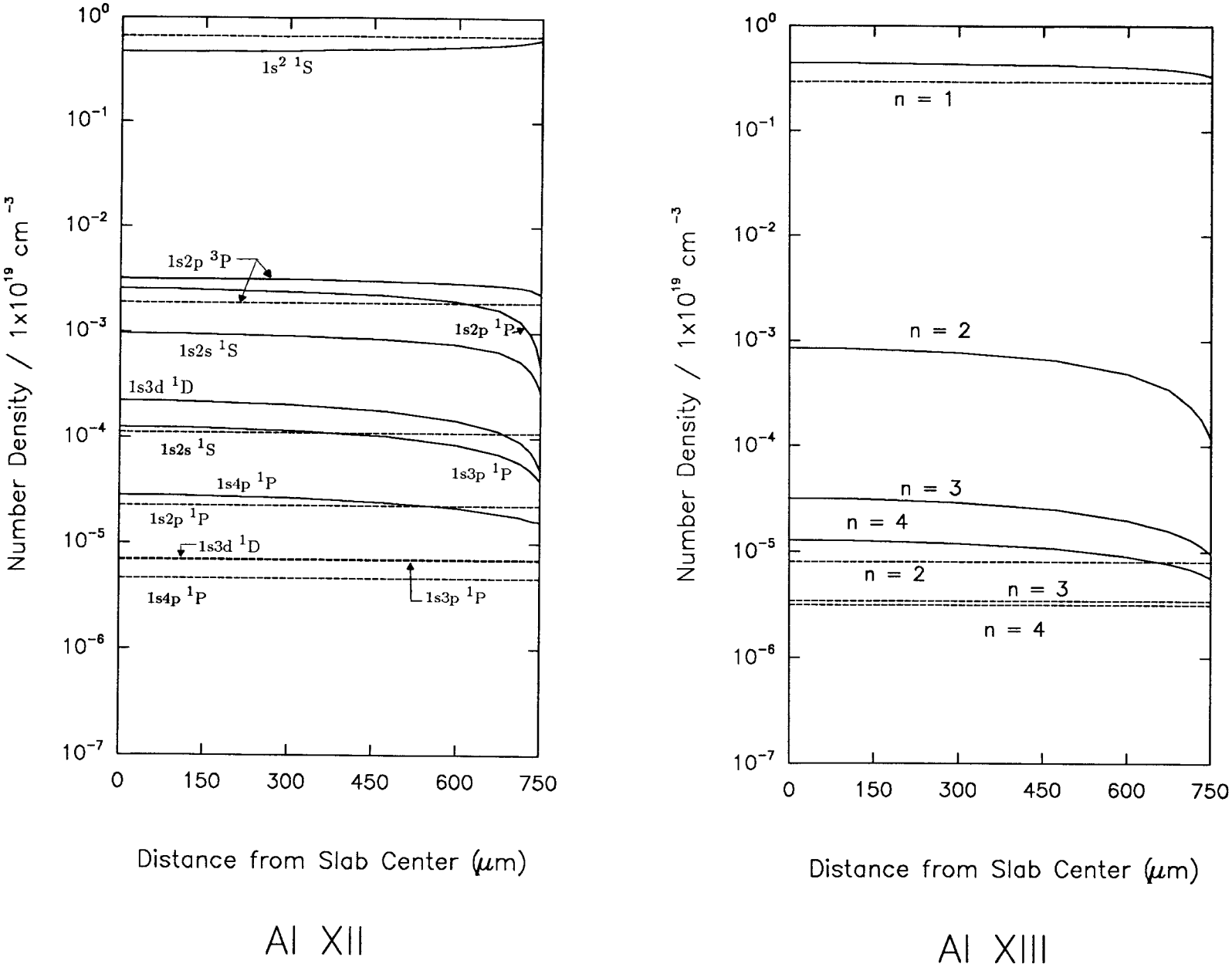

Figure 10. Level population distributions in a 0.15 cm-thick Al plasma slab with $T_e = 600eV$ and $n = 1x10^{19}\text{cm}^{-3}$. Dashed lines indicate optically thin populations.

to/from the ground state involves a change in the spin state.

Also shown in Figure 10 are the populations for an optically thin Al plasma at the same density and temperature (dashed lines). In this case, the photoexcitation rates are assumed to be zero and the populations are independent of the radiation field. Comparison of the optically thin and optically thick results shows that the radiation field can significantly alter the populations of the excited states. For instance, the 1s 2p ^{1}P (Al XII) and $n = 2$ (Al XIII) populations are roughly 2 orders of magnitude higher near the slab center for the optically thick case.

Figure 11 shows the total line power coefficients ($\Lambda = P_{bb}/n_e n_{tot}$) for optically thin Al plasmas as a function of electron temperature for densities ranging from 10^{13} to 10^{21} ions/cm^3. At low densities ("coronal" regime; $n \ll 10^{15}$ cm^{-3}), the power coefficient becomes independent of density because the collisional deexcitation and recombination rates become much smaller than their radiative counterparts. As the density increases, the excited state populations decline due to the increased importance of collisionally-induced downward transitions. Oscillations in the line power coefficient curve results from the electronic shell structure of the ions.

Reabsorption effects in optically thick plasmas can be seen in Figure 12. Here, the total line power for an Al plasma cylinder with $n = 1 \times 10^{19}$ ions/cm^3 is plotted as a function of electron temperature. The line profiles in this calculation were assumed to be Voigt profiles. As the radius of the cylinder is increased from 0 (optically thin case) to 5000 μm, the total line power decreases by as much as an order of magnitude. This is because line center optical depths become large (up to $\sim$ several hundred for $R = 5000$ μm) and photons emitted from within the plasma interior are "destroyed" before they can escape.

To assess the reliability of our radiative transfer computer code, we have compared the Al plasma results with previously published results. Figures 13, 14, and 15 show results from Refs. [2] and [3], which were obtained using a similar escape probability

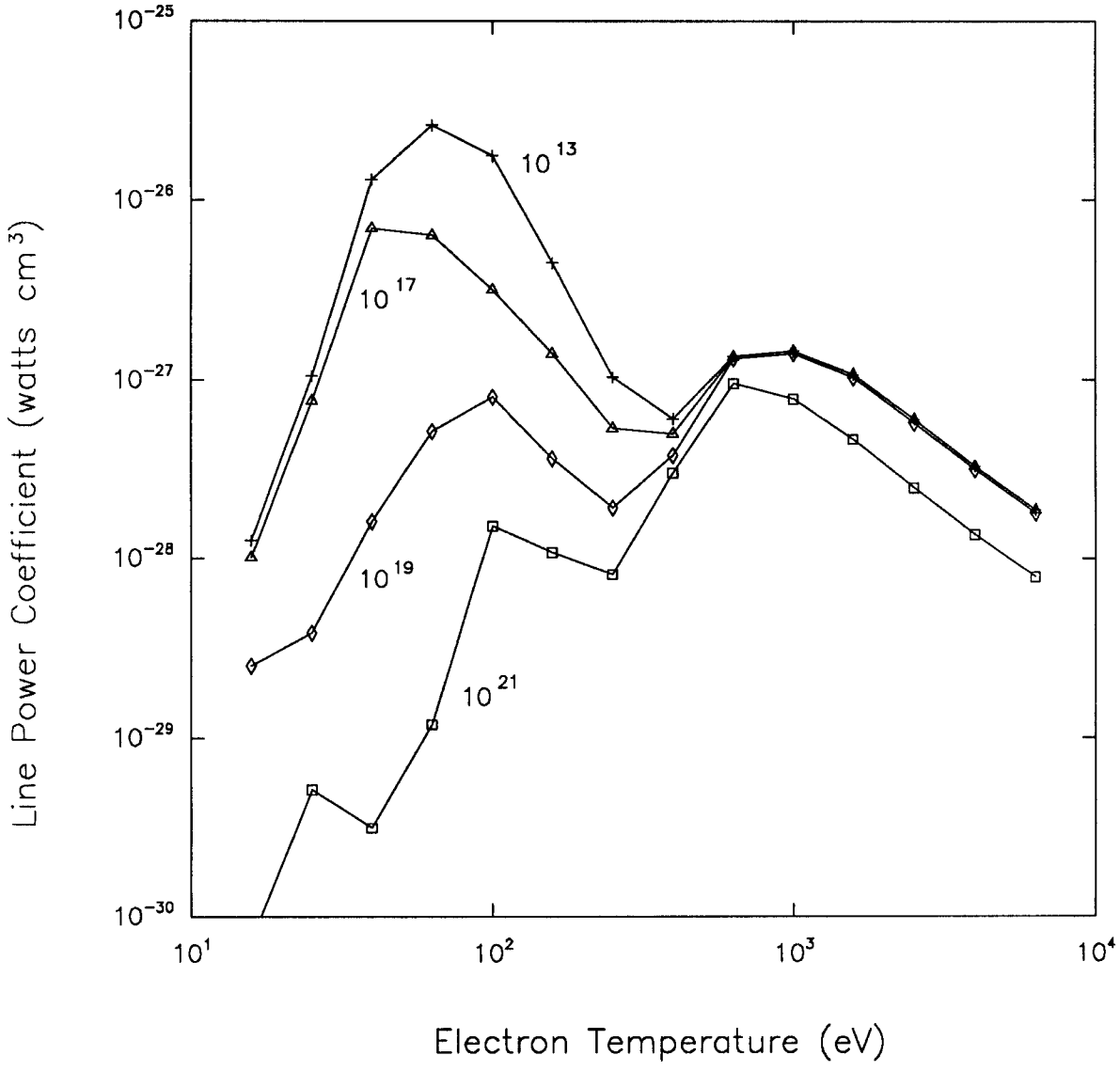

Figure 11. Total line emission power coefficients of optically thin Al plasmas for ion densities ranging from 10^{13} cm^{-3} to 10^{21} cm^{-3}.

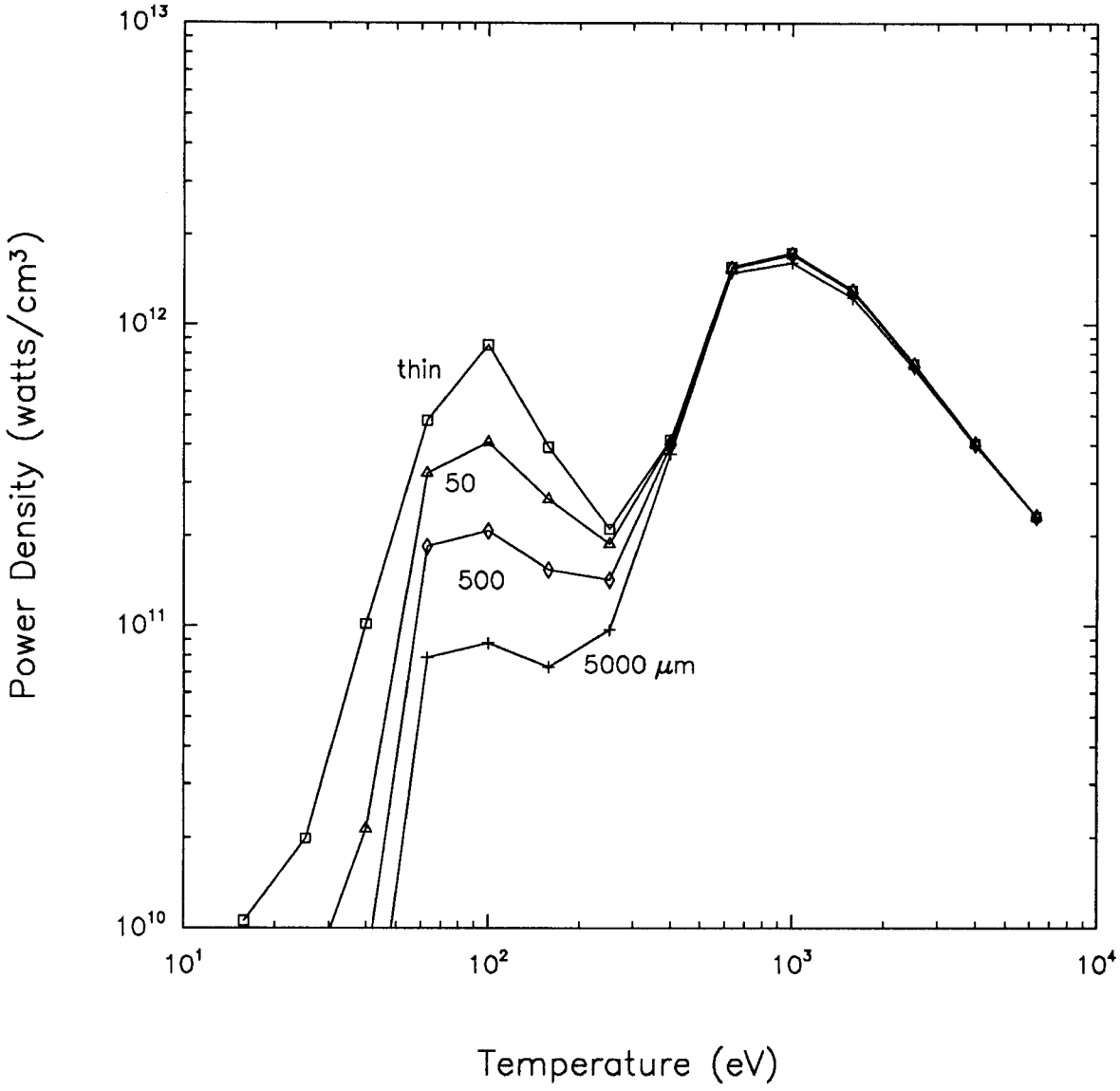

Figure 12. Total line emission power densities of optically thick Al plasma cylinders with $n = 1 \times 10^{19}$ ions/cm^3 and cylinder radii of $R = 0$ (top; thin plasma), 50, 500, and 5000 μm (bottom).

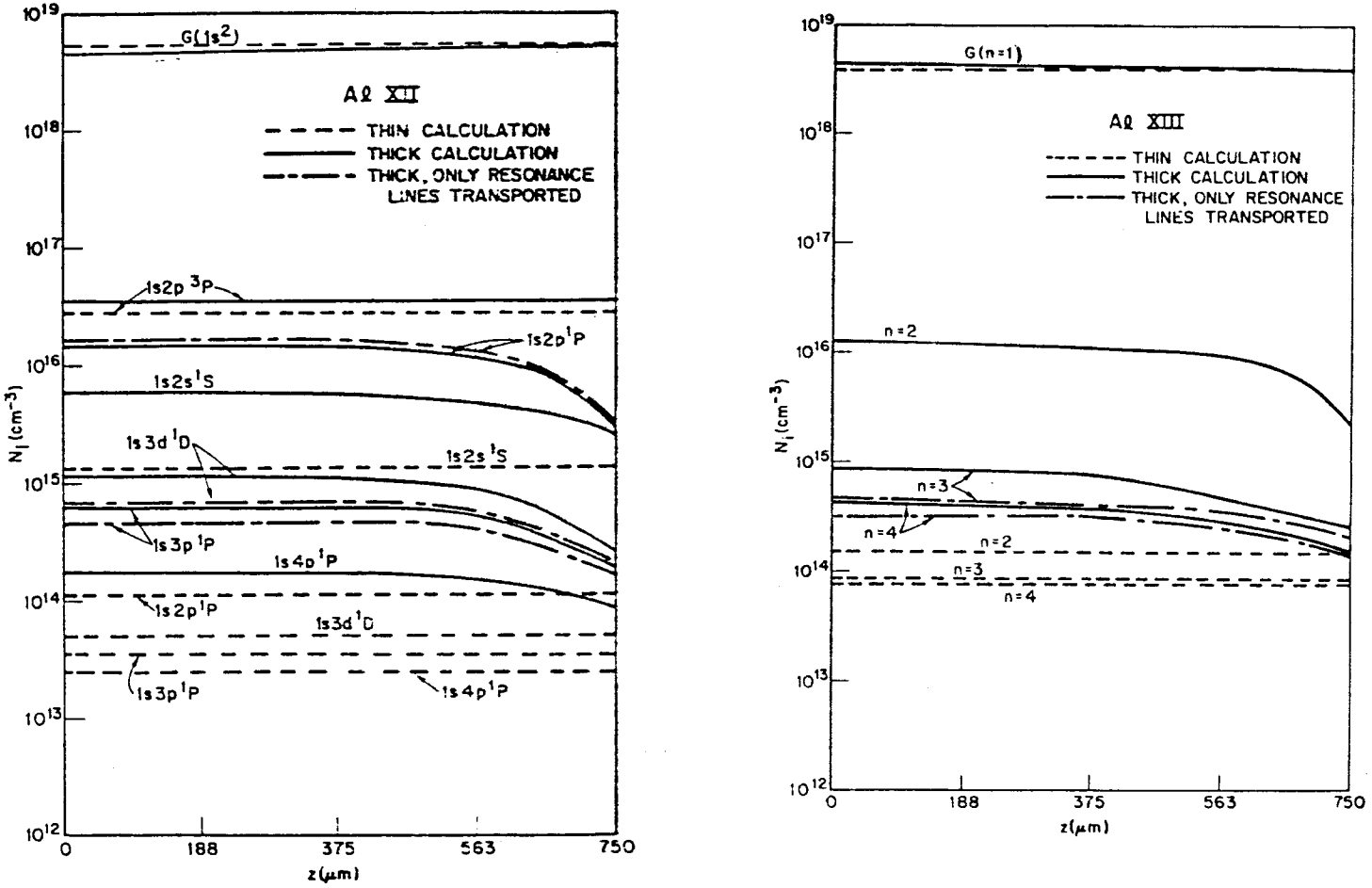

Figure 13. Excited and ground state densities of Al XII and Al XIII from calculation by Apruzese et al. [2]. Compare with Fig. 10.

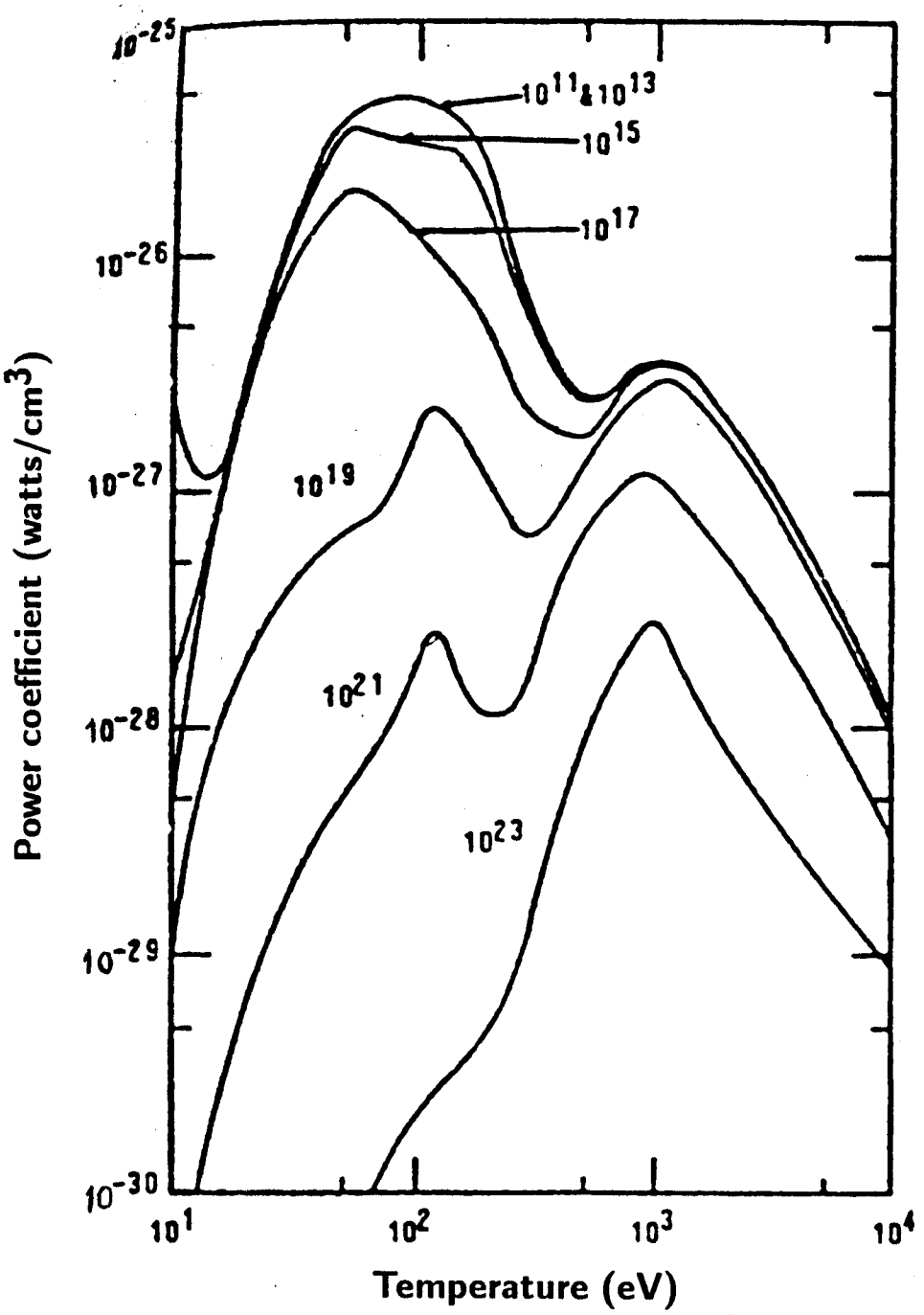

Figure 14. Total line emission power coefficients for optically thin Al plasmas calculated by Duston and Davis [3]. Compare with Fig. 11.

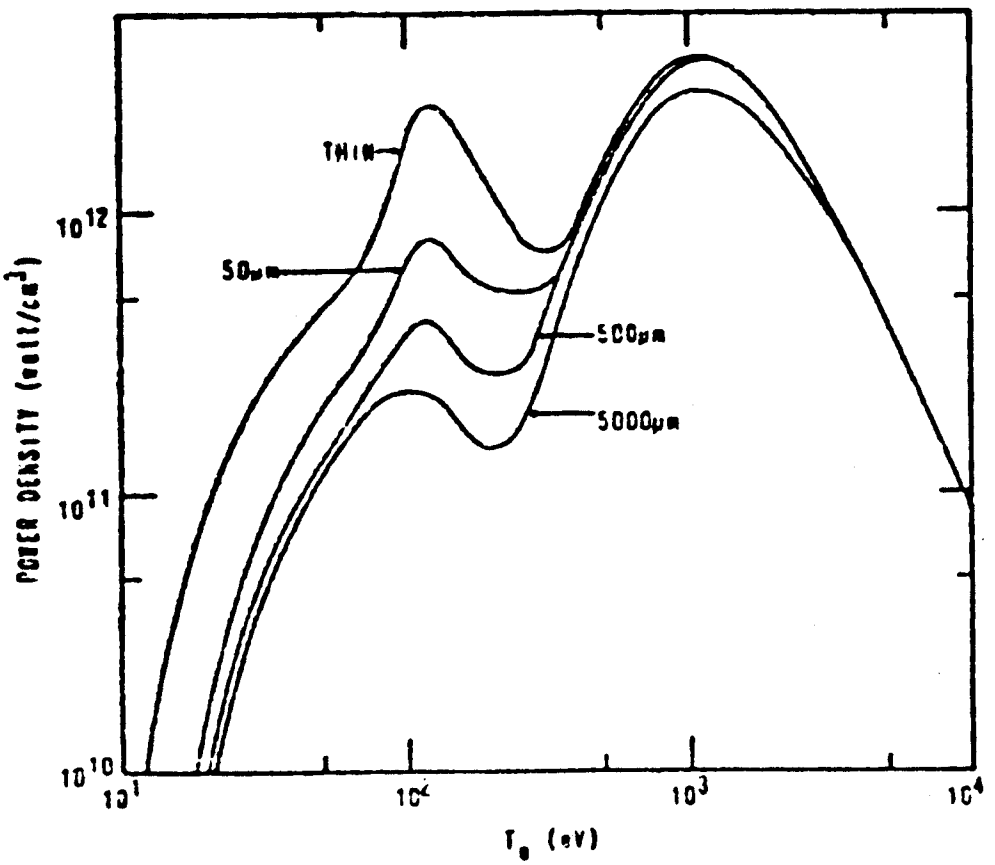

Figure 15. Total line emission power densities for optically thick cylindrical Al plasmas calculated by Duston and Davis [3]. Compare with Fig. 12.

radiative transfer model. These results can be compared with those in Figures 10 through 12. In each case, the results from the different two calculations are in good agreement. Discrepancies between the two calculations are typically $\sim$ a factor of a few in absolute power density. These are due primarily to differences in the atomic data used. This can be seen by comparing the results from optically thin calculations in which radiative transfer effects are neglected. For instance, the line power coefficient for Al at $T = 100$ eV and $n = 10^{19}$ cm^{-3} is 8.0×10^{-28} watts cm^3 in our calculations (Fig. 11), versus about 2.5×10^{-27} in the calculations by Duston and Davis [3] (Fig. 14). We feel our results may in fact be more reliable because they are based on more detailed atomic physics models, while the calculations of Ref. [3] used rate coefficients based on simpler (e.g., hydrogenic ion) models. (Duston and Davis pointed out the shortcomings of this data and emphasized this importance of using reliable atomic physics data in a subsequent paper [23].) Similar differences appear in the population distributions (Fig. 10 vs. Fig. 13) and the power densities for optically thick plasmas (Fig. 12 vs. Fig. 15). Note, however, that the qualitative features of the two sets of results are quite similar. For instance, the relative positions of the level populations with respect to one another and the population gradients agree rather well. Also, the importance of reabsorption of line radiation at temperatures below about 300 eV is apparent in both calculations (Figs. 12 and 15). We feel the good overall agreement between our results and those from previous calculations indicates that our radiative transfer model is working reliably.

We have also compared our results with multigroup radiation diffusion calculations. Figure 16 shows the power density (scaled to the optically thin value to mitigate differences in atomic data) for an Al cylindrical plasma with a radius ranging from 50 to 5000 μm. In each case the plasma has a uniform temperature of 100 eV and density of 10^{19} ions/cm^3. The multigroup diffusion power densities (dotted curve) are about a factor of 2 and 4 higher than the non-LTE escape probability results for plasma radii of 50 and 5000 μm, respectively. This suggests that radiation diffusion calculations,

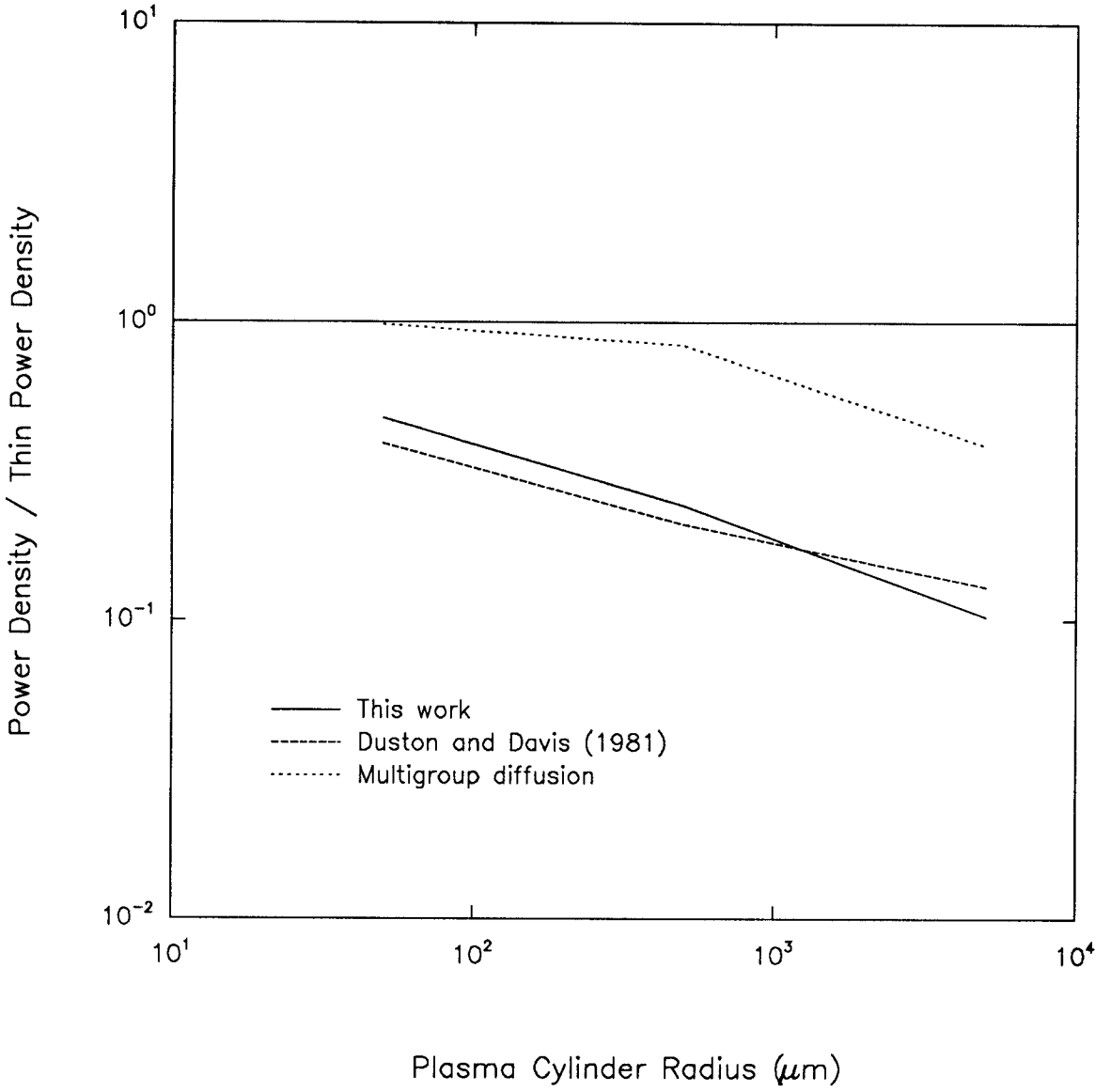

Figure 16. Comparison of scaled power densities computed using non-LTE escape probability model and multigroup radiation diffusion model. Calculations are for cylindrical Al plasmas at $T = 100$ eV and $n = 10^{19}$ ions/cm^3.

which do not consider the influence of the radiation field on the atomic populations, can significantly overestimate the radiation flux escaping the plasma. Also shown are the scaled power densities from Ref. [3], which are seen to be in good agreement with our calculations.

We have performed a similar set of calculations for spherical Ne plasmas at lower densities. The plasmas were again optically thick because the plasma volumes were much larger than those in the Al calculations. The conditions considered in these calculations are similar to those expected for ICF Z-pinch plasma channels (used for transporting an ion beam from the diode to the target) and target chamber microfireballs.

Results from the Ne calculations are shown in Figs. 17 through 21. The major conclusions are as follows:

1. The total line power density is significantly lower than the optically thin power densities at $T \leq 100$ eV and $R \geq 1$ cm (Fig. 20). This suggests that reabsorption of line radiation may be very important in ICF target chamber plasmas (both Z-pinches and microfireballs). This is especially significant because bound-bound transitions are the dominant contributor to the total plasma emission rate at these densities.
2. The power densities predicted by the non-LTE escape probability model are significantly lower (as much as an order of magnitude) than those predicted from multigroup radiation diffusion methods (Fig. 21). This suggests that diffusion models underestimate the effects of reabsorption of line radiation for plasma conditions expected for ICF target chambers.

These conclusions, though preliminary, may have important implications for transporting light ion beams to ICF targets. For example, in the LIBRA design study [24], a background gas of He was used because it was predicted that higher-Z gases would not produce sufficiently strong magnetic fields to confine the ion beam. This conclusion was based on radiation-magnetohydrodynamics calculations which predicted that radiatively-driven expansion (RDE) in higher-Z plasma channels leads to weaker

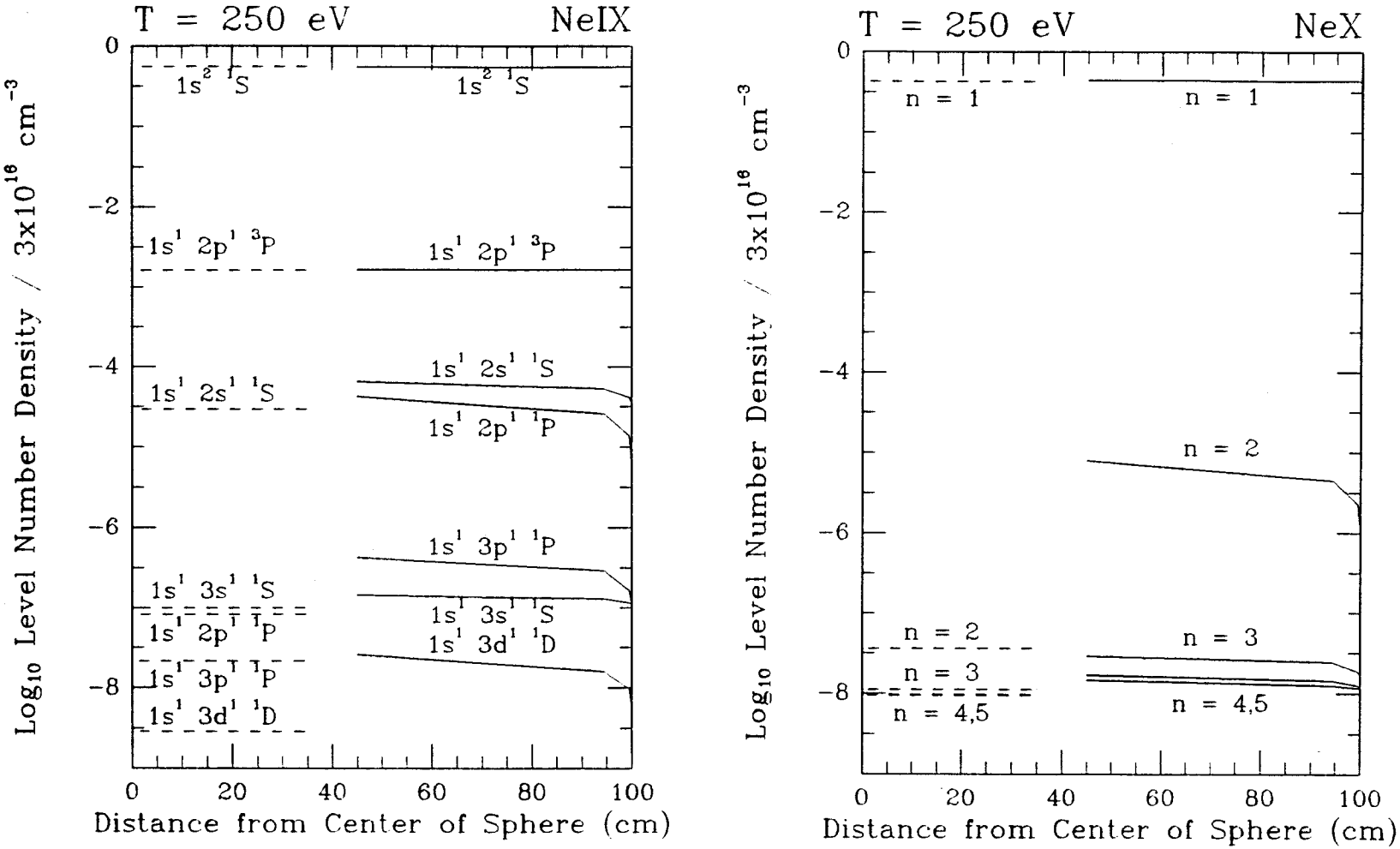

Figure 17. Level population distributions in a Ne plasma sphere of 1 meter radius with $T_e = 250$ eV and $n = 3 \times 10^{16}$ cm^{-3}. Levels considered were similar to He-like and H-like stages in Fig. 9. Dashed lines indicate optically thin populations.

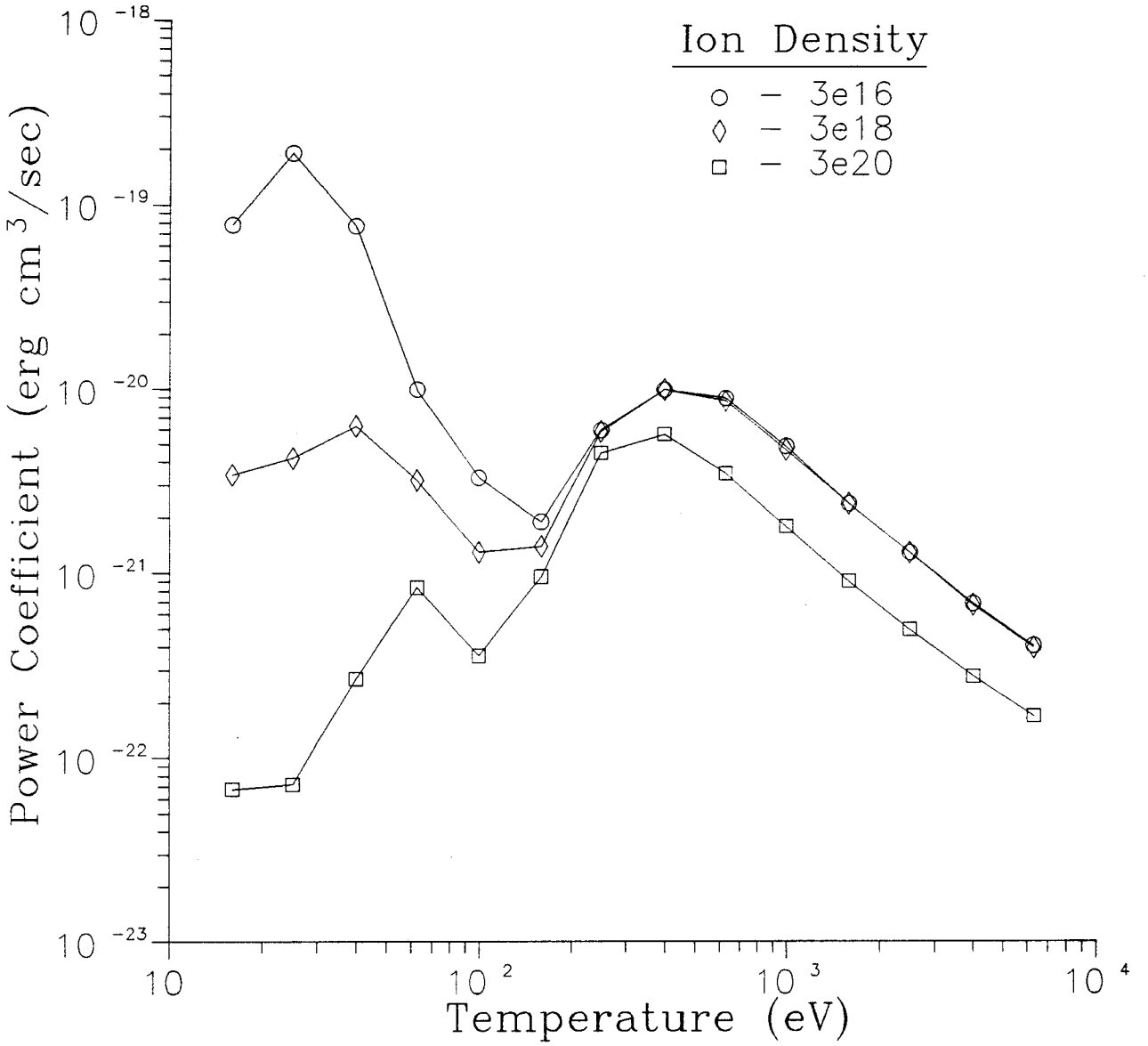

Figure 18. Total line emission power coefficients of optically thin Ne plasmas at densities of 3×10^{16} (top), 3×10^{18}, and 3×10^{20} cm^{-3} (bottom).

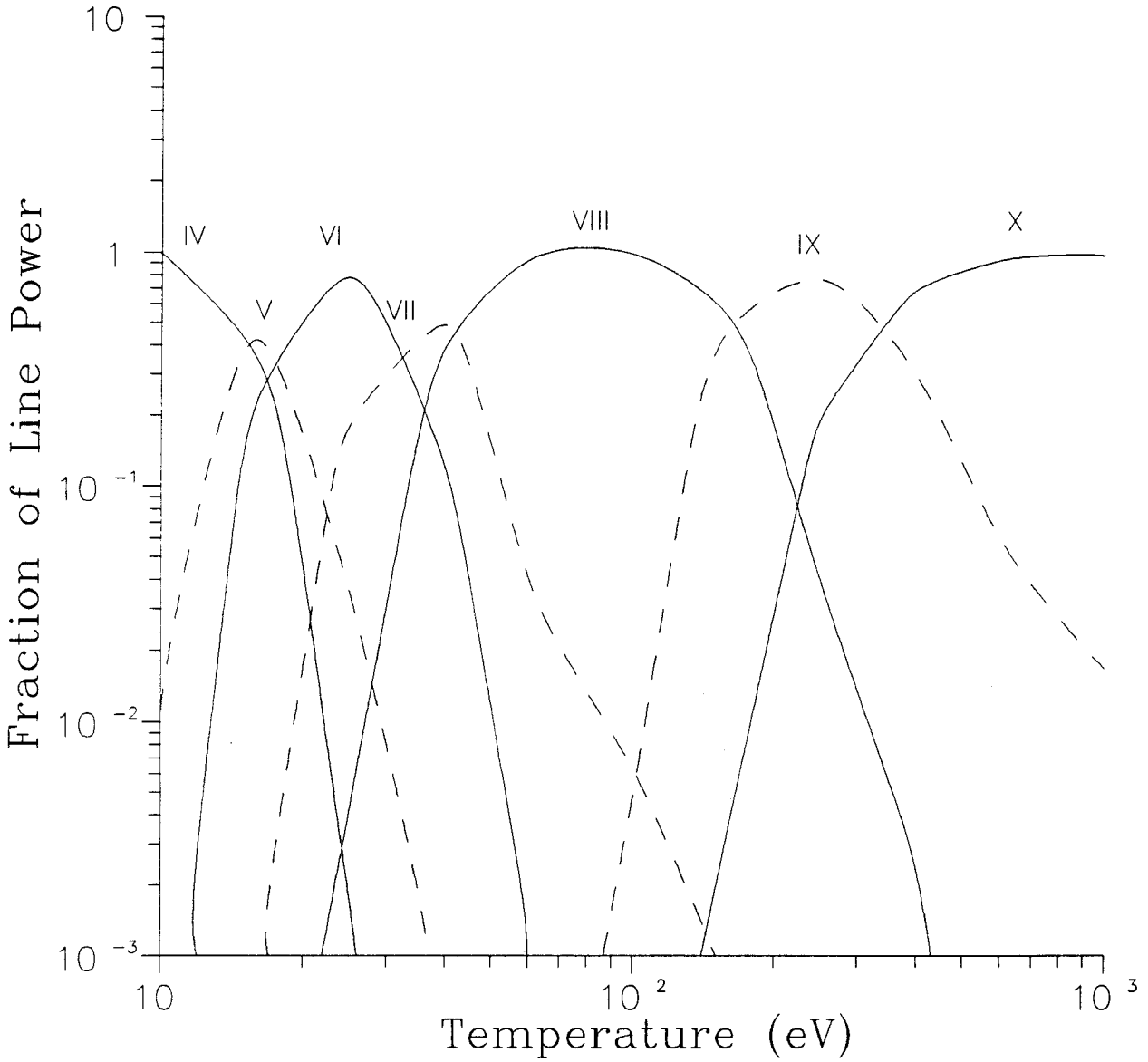

Figure 19. Contribution to total line power coefficient from each Ne ion. Optically thin case with $n = 3 \times 10^{16}$ cm^{-3}.

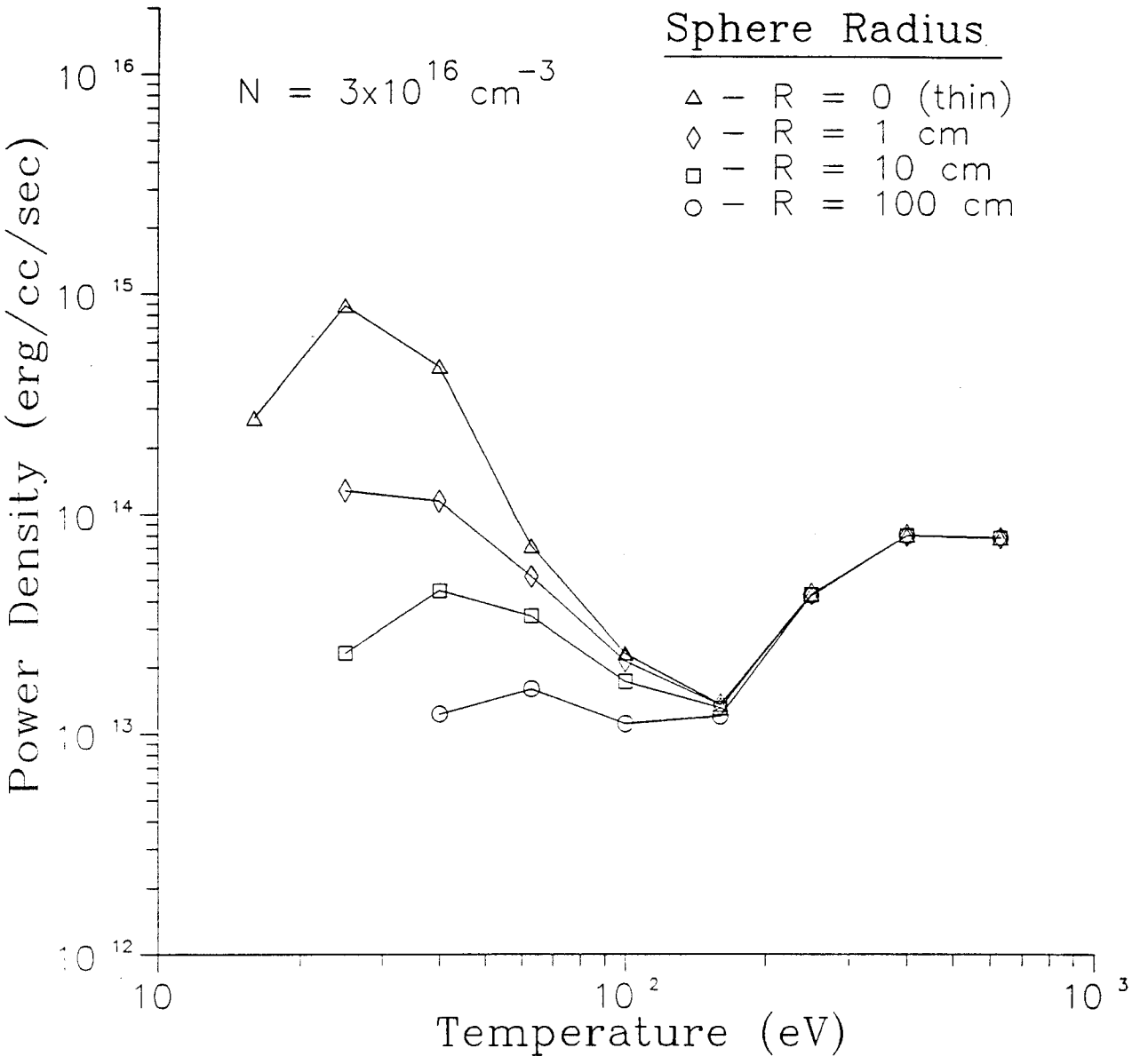

Figure 20. Total line emission power densities for optically thick Ne plasma spheres. The ion density in each case was 3×10^{16} cm^{-3}. The line optical depths increase as the sphere radius increases, leading to a reduction in the power density.

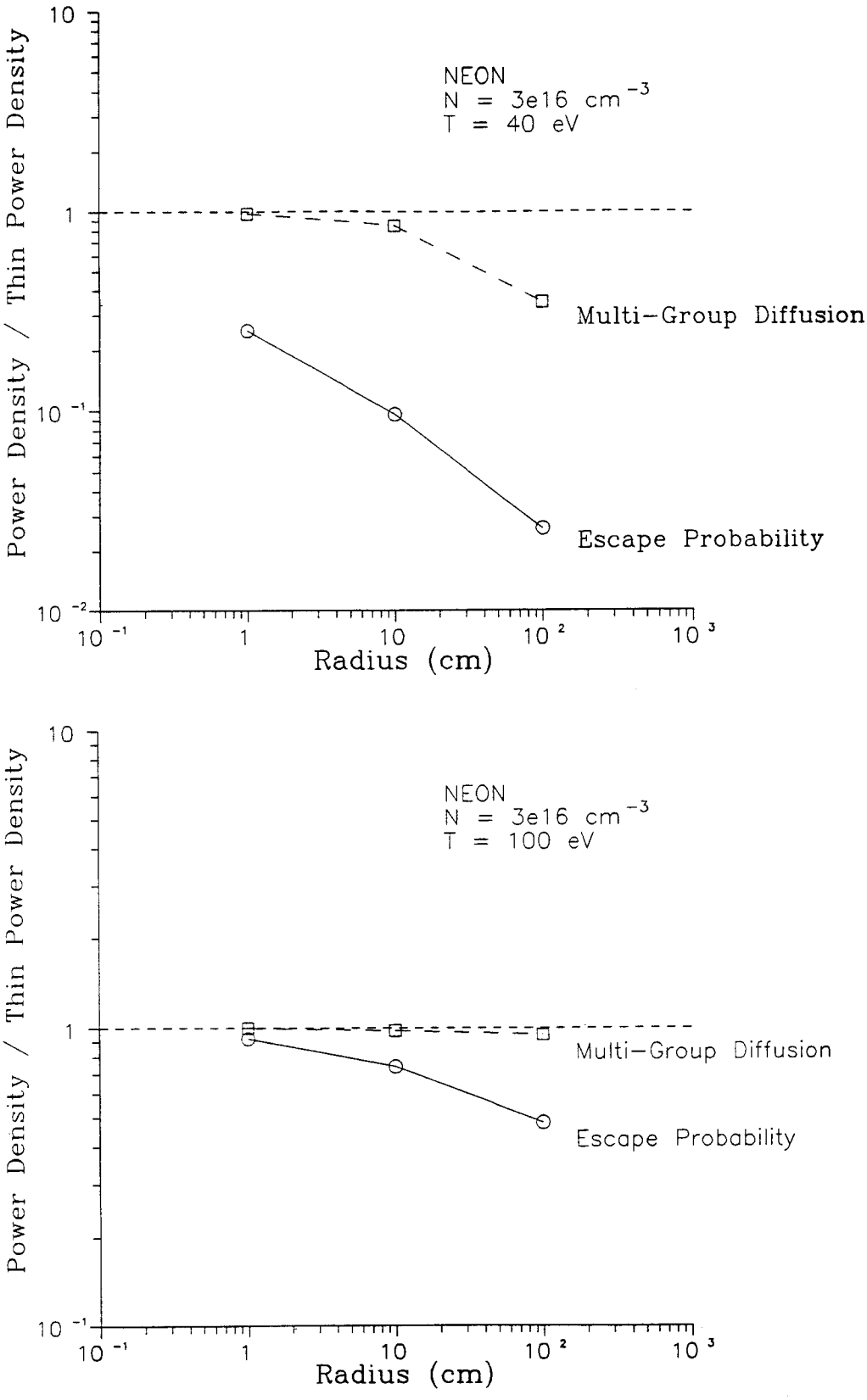

Figure 21. Comparison of scaled power densities computed using non-LTE escape probability and multigroup radiation diffusion transport models. Calculations are for spherical Ne plasmas at $T = 40$ and 100 eV with $n = 3 \times 10^{16}$ cm^{-3}. Note that diffusion models can dramatically underestimate effects of reabsorption for these conditions.

magnetic fields. Radiation was transported in these calculations using a multigroup radiation diffusion model. However, our escape probability calculations now suggest that reabsorption of line radiation may significantly reduce RDE effects and result in stronger magnetic fields for high-Z gases. It would be advantageous to use higher-Z gases to transport ion beams to the target because the gas would provide significantly greater protection for the chamber walls and INPORT tubes from the target x-rays. Our non-LTE results also suggest that the radiative flux from microfireballs will also be lower than predicted from radiation diffusion models. This would reduce the heat flux and the potentially damaging thermal stresses on the first wall in many target chamber designs. Thus, line reabsorption may provide a very beneficial protection mechanism for ICF target chambers.

4. SUMMARY AND FUTURE DIRECTIONS

We have presented a detailed description of an escape probability radiative transfer model that can be used to simulate the radiative properties of non-LTE plasmas. The major features of the model are: (1) multilevel atomic rate equations are solved self-consistently with the radiation field; (2) escape factors are used to predict high-resolution spectra escaping from a plasma, thus providing a powerful diagnostic capability for laboratory plasmas; and (3) the method for solving the coupled rate equations is computationally efficient, so that the model can be incorporated into radiation-hydrodynamics codes to study time-dependent conditions of rapidly changing plasmas.

Results of our calculations have been compared with a variety of other calculations. Comparisons with exact solutions for 2-level atoms have shown that the angle- and frequency-averaging techniques employed to provide a high degree of computational efficiency lead to only a modest sacrifice in accuracy. We have also compared our results for multilevel plasmas with previously published calculations which used very similar methods and found good agreement. Finally, major differences were found between

results from our escape probability model and multigroup radiation diffusion calculations. We argue that for some plasma conditions, multigroup diffusion models can overestimate the radiative flux escaping a non-LTE plasma by more than an order of magnitude.

Currently, our escape probability code can be used to study isothermal, isochoric, multilevel plasmas in planar, cylindrical, and spherical geometries. There are several features we would like to add to the model before it is coupled to radiation-hydrodynamics codes. These are:

(1) Include temperature and density gradient effects in computing the escape probabilities and coupling coefficients.

(2) Include effects of Doppler shifting (i.e., velocity gradients). This is because as plasmas expand, Doppler shifting of lines can reduce the amount of reabsorbed radiation.

(3) Improve convergence rate and robustness of solutions. Apruzese et al. [8] have employed methods to accelerate convergence of solutions. In addition, it may prove fruitful to explore, using numerical techniques that have recently been developed, non-LTE radiative transfer in astrophysical plasmas [16-18].

(4) Include cross-coupling effects between different transitions; e.g., allow for attenuation of line photons by photoabsorptions (such as Auger ionizations in a cooler part of a plasma).

When completed, the model will be ready to be coupled with existing radiation-hydrodynamics codes.

ACKNOWLEDGEMENTS

The authors gratefully acknowledge support from Kernforschungszentrum Karlsruhe (KfK) through Fusion Power Associates. Computing support has been provided in part by the U.S. National Science Foundation through the San Diego Supercomputing Center.

REFERENCES

1. Mihalis, D., Stellar Atmospheres, Second Edition (Freeman, New York, 1978).
2. Apruzese, J.P., Davis, J., Duston, D., and Whitney, K.G., *J.Q.S.R.T.* **23**, 479 (1980).
3. Duston, D. and Davis, J., *Phys. Rev. A* **23**, 2602 (1981).
4. Duston, D., Clark, R.W., Davis, J., and Apruzese, J.P., *Phys. Rev. A* **27**, 1441 (1983).
5. MacFarlane, J.J., Wang, P., Yasar, O., and Moses, G.A., Bull.Amer.Phys.Soc. **34**, 2151 (1989).
6. Apruzese, J.P., *J.Q.S.R.T.* **25**, 419 (1981).
7. Apruzese, J.P., *J.Q.S.R.T.* **34**, 447 (1985).
8. Apuzese, J.P., Davis, J., Duston, D., and Clark, R.W., *Phys. Rev. A* **29**, 246 (1985)
9. Holstein, T., *Phys. Rev.* **72**, 1212 (1947).
10. Athay, R.G., *Ap. J.* **176**, 659 (1972).
11. Jeffries, J.T., Spectral Line Formation (Waltham, Blaisdel, 1968).
12. Averett, E.H., and Hummer, D.G., *M.N.R.A.S.* **130**, 295 (1965).
13. Avery, E.H., House, L.L., and Skumanich, A., *J.Q.S.R.T.* **9**, 519 (1969).
14. Kunasz, P.B., and Hummer, D.G., *M.N.R.A.S.* **166**, 19 (1974).
15. LINPACK Users Guide, edited by J.J. Dongarra et al. (SIAM, Philadelphia, 1979).
16. Scharmer, G.B. and Carlsson, M., *J. Comput. Phys.* **59**, 56 (1985).
17. Werner, K., *Astron. Astrophys.* 161, 177 (1986).
18. Klein, R.I., Castor, J.I., Greenbaum, A., Taylor, D., and Dykema, P.G., *J.Q.S.R.T.* **41**, 199 (1989).
19. Wang, P., Ph.D. Dissertation, University of Wisconsin, in preparation.
20. Burgess, A. and Summer, H.P., *M.N.R.A.S.* **174**, 345 (1976)
21. Sobelman, I.I., Excitation of Atoms and Broadening of Spectral Lines (Springer-Verlag, New York, 1981).

22. Post, D.E., Jensen, R.V., Tarter, C.B., Grasberger, W.H., and Lokke, W.A., *At. Data Nucl. Data Tables*, **20**, 397 (1977).

23. Duston, D. and Davis, J., *J.Q.S.R.T.* **27**, 267 (1982).

24 Moses, G.A., et al., Proceedings of Beams '88 Conference, Karlsruhe, FRG.